

# We are IntechOpen, the world's leading publisher of Open Access books Built by scientists, for scientists

6,900

Open access books available

185,000

International authors and editors

200M

Downloads

Our authors are among the

154

Countries delivered to

TOP 1%

most cited scientists

12.2%

Contributors from top 500 universities



WEB OF SCIENCE™

Selection of our books indexed in the Book Citation Index  
in Web of Science™ Core Collection (BKCI)

Interested in publishing with us?  
Contact [book.department@intechopen.com](mailto:book.department@intechopen.com)

Numbers displayed above are based on latest data collected.  
For more information visit [www.intechopen.com](http://www.intechopen.com)



---

# Plasmonic Lenses

---

Yongqi Fu, Jun Wang and Daohua Zhang

Additional information is available at the end of the chapter

<http://dx.doi.org/10.5772/50029>

---

## 1. Introduction

The resolution of almost all conventional optical system is indispensably governed by the diffraction limit. This resolution limit can be overcome by use of focusing the evanescent waves in the near field region. The concept of “superlens” was proposed firstly by Pendry in 2000 [1]. When  $\epsilon = -1$  and  $\mu = -1$ , the negative refractive index material plate can be a perfect lens [2-4]. Because of the dispersion and absorption in the materials, the conditions of  $\epsilon = -1$  and  $\mu = -1$  is hard to satisfy for the natural materials. Although the perfect lens may not exist, the superlens which can provide higher resolution beyond the diffraction limit have been proved. And focusing by means of surface plasmon polaritons (SPPs) by plasmonic lens is attracting much interest recently due to its unique feature of extraordinary enhanced transmission [5-8]. It means that we can focus the evanescent components of an illuminated object in the near-field region with subdiffraction-limit resolution [9]. This allows them to break the conventional barrier of diffraction limit, and leads to the formation of concentrated sub-wavelength light spots on the order of nanometers. Plasmonic lens is always consisted by metal and dielectric and can excite SPPs and always can be used for focusing, imaging, and beam shaping and so on.

In this paper, a literature review is given for the purpose of displaying a physical picture of plasmonic lenses for the relevant reader. Firstly, the basic theory about the plasmonic lens is presented. Then several examples of plasmonic lens are given. Here we mainly focus on the typical concepts of the plasmonic lens reported so far.

## 2. Plasmonic lens on the basis of negative refractive index materials

### 2.1. Superlens

Although perfect lens proposed by Pendry may not exist, superlens is realized and proved by Zhang's group in 2003 [10-13] and other research groups [14-21]. Here we mainly introduce the typical works which were done by Zhang's group. They showed that optical

evanescent waves could indeed be enhanced as they passed through a silver superlens. Figure 1 below shows configuration of the superlens they designed.

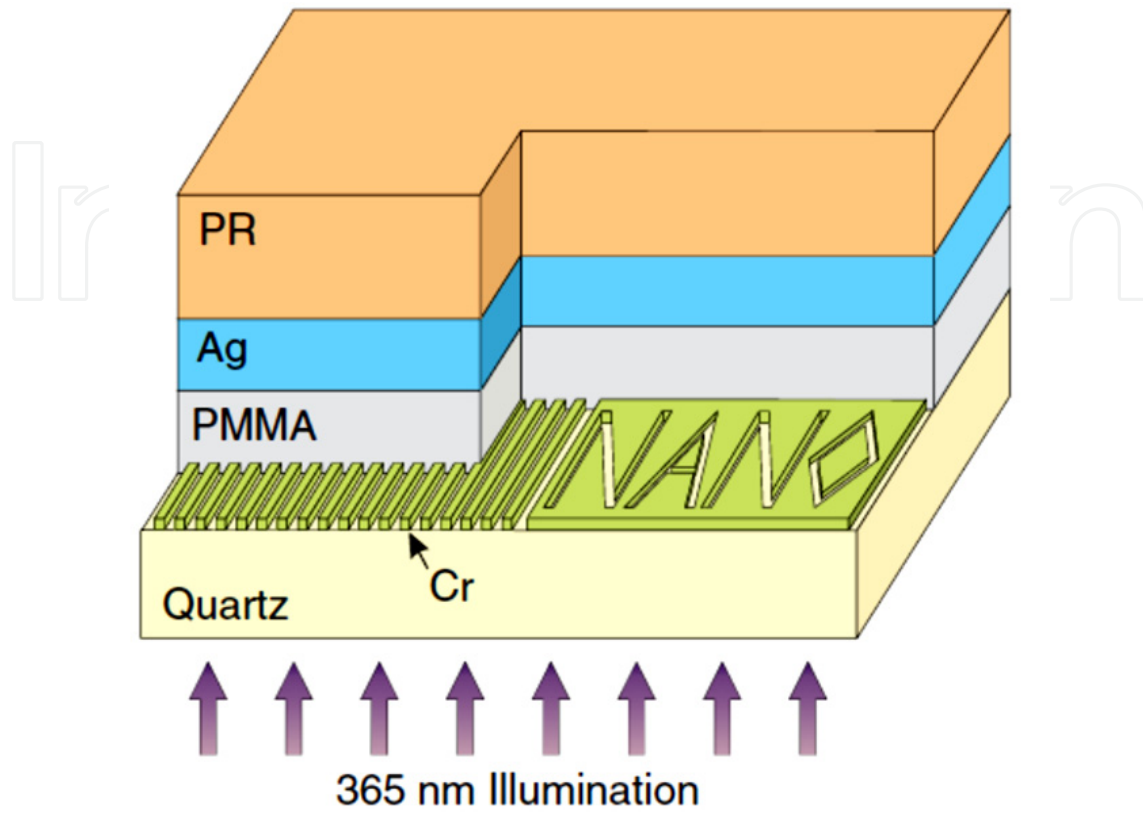


**Figure 1.** Optical superlensing designed by Zhang's group. Reprinted with permission from "N. Fang, H. Lee, C. Sun and X. Zhang, *Science* 308, 534-537 (2005)." of copyright ©2005 American Institute of Physics.

As can be seen, a set of objects were inscribed onto a chrome screen. The objects were designed to be placed about 40 nm away from the silver film which is 35 nm in thickness. And the chrome objects were patterned on quartz by using focused ion beam (FIB) technique, a 40 nm thick layer of polymethyl methacrylate (PMMA) was used to planarize them. The objects are imaged onto the photoresist on the other side of the silver film under ultraviolet (UV) illumination (at a wavelength of 365 nm). The negative photoresist which is 120 nm thick is used to record the near-field image. The substrate is flood-exposed under an I-line (365 nm) mercury lamp. The exposure flux is 8 mW/cm<sup>2</sup>, and an optimal exposure time of 60 s is applied to reduce the surface root mean square modulation below 1 nm for both the silver and PMMA surfaces; otherwise, the dispersion characteristics of the superlens would be modified and would in turn smear the details of the recorded image. The optical image is converted into topographic modulations by developing the negative photoresist and is mapped using atomic force microscopy (AFM).

Because the electric and magnetic responses of materials were decoupled in the near field, only the permittivity needs to be considered for transverse magnetic (TM) waves. This makes noble metals such as silver natural candidates for optical superlensing. Silver is chosen here. As surface charges accumulate at the interface between the silver and the imaging medium, the normal component of an electric of silver is selected and the permittivity of the silver and

that of the adjacent medium are equal and of opposite sign. Such a delicate resonance is essential to ensure the evanescent enhancement across the slab. For enhanced transmission of evanescent waves, it is found that an asymptotic impedance match ( $k_{zi} / \epsilon_i + k_{zj} / \epsilon_j = 0$ ) has to be met at the surface of the silver, known as the surface plasmon excitation condition ( $k_{zi}$ , cross-plane, wave vector in silver;  $\epsilon_i$ , permittivity of silver;  $k_{zj}$ , cross-plane wave vector in dielectric; and  $\epsilon_j$ , permittivity of dielectric). It is widely known in metal optics that when the two media take the opposite sign in permittivity and  $|\epsilon_i| \gg \epsilon_j$ , only surface plasmons at the narrow range of in-plane wave vector ( $k_x$ ) that are close to  $k_0$  can be resonantly coupled. However, less well known is that when  $|\epsilon_i| \sim \epsilon_j$  and we are of opposite sign, the excitable surface plasmon band of  $k_x$  is significantly broadened, resulting in the superlensing effect.

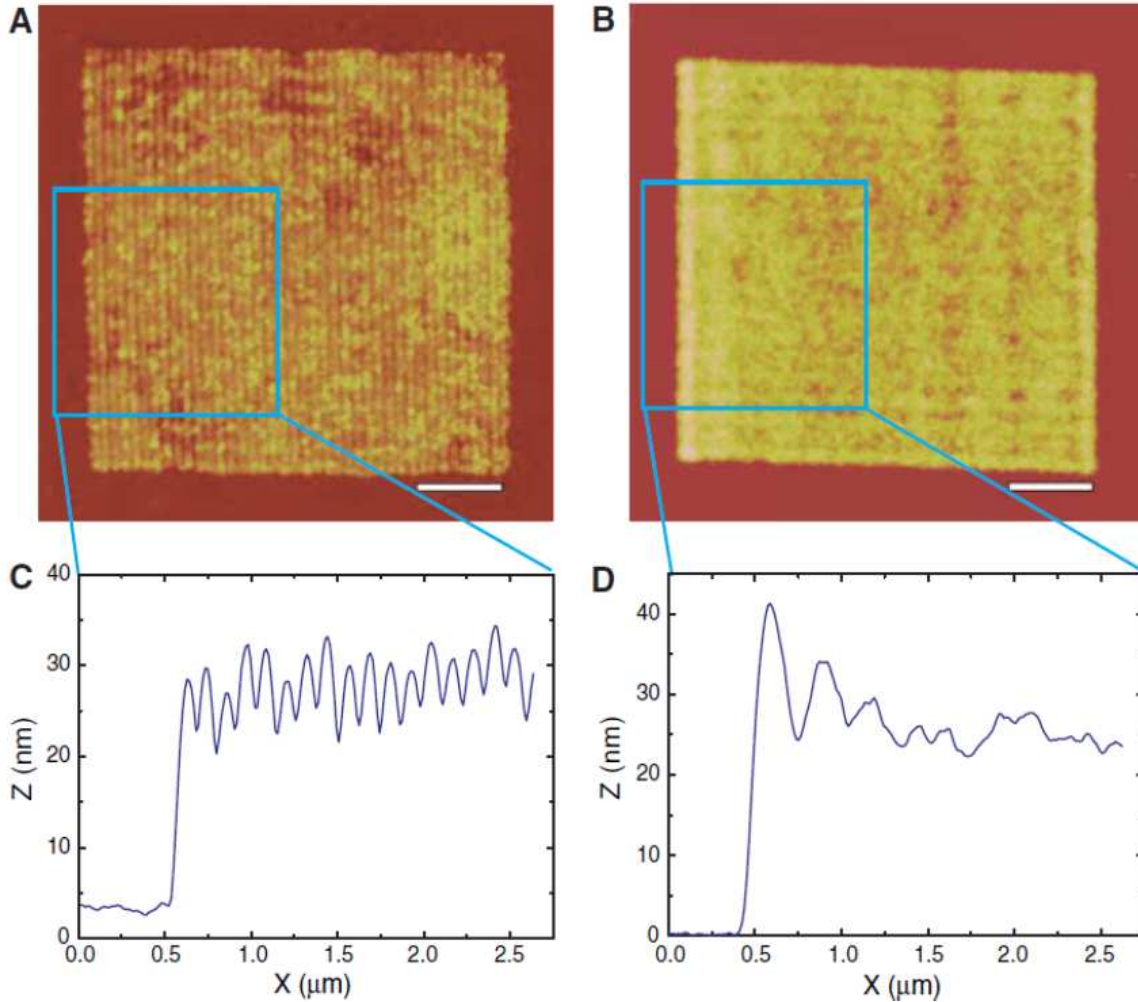


**Figure 2.** (A) AFM of the developed image (scale bar, 1  $\mu\text{m}$ ; color scale from dark red to bright yellow, 0 to 150 nm). (B) Control experiments were carried out, in which the silver superlens layer was replaced by a 35 nm thick PMMA layer, for a total PMMA thickness of 75nm. (C) The blue solid curve shows the clearly demonstrating the  $63 \pm 4$  nm half-pitch resolved with a 35 nm silver superlens. X direction is relative displacement along the cross-section direction. (D) The blue solid curve shows the average cross section of Fig. 2B (control sample). Reprinted with permission from "N. Fang, H. Lee, C. Sun and X. Zhang, Science 308, 534-537 (2005)." of copyright ©2005 American Institute of Physics.

The intensity of evanescent waves decays with a characteristic length  $Z$ , and

$$Z^{-1} = 4\pi\sqrt{a^{-2} - \varepsilon\lambda^{-2}}, \quad (1)$$

where  $a$  is the period of a line array, and  $\varepsilon$  is the permittivity of the surrounding media. In Zhang's experiment, for the 60 nm half-pitch and  $\varepsilon = 2.4$ , the decay length is estimated to be 11 nm. Thus it is obviously difficult to resolve a 60 nm half-pitch object from a distance of 75 nm away if there isn't a superlens to enhance and transmit the evanescent waves. So we could find the photoresist images with typical average height modulations of 5 nm to 10 nm from Fig. 2 C. And this is assisted by careful control of the surface morphology of the PMMA and silver surface. In addition, Zhang also proved that the silver superlens can also image arbitrary nanostructures with sub-diffraction-limited resolution. The recorded image "NANO" in Fig. 3 B shows that the fine features from the mask showed in Fig. 3 A in all directions with good fidelity can be faithfully produced.

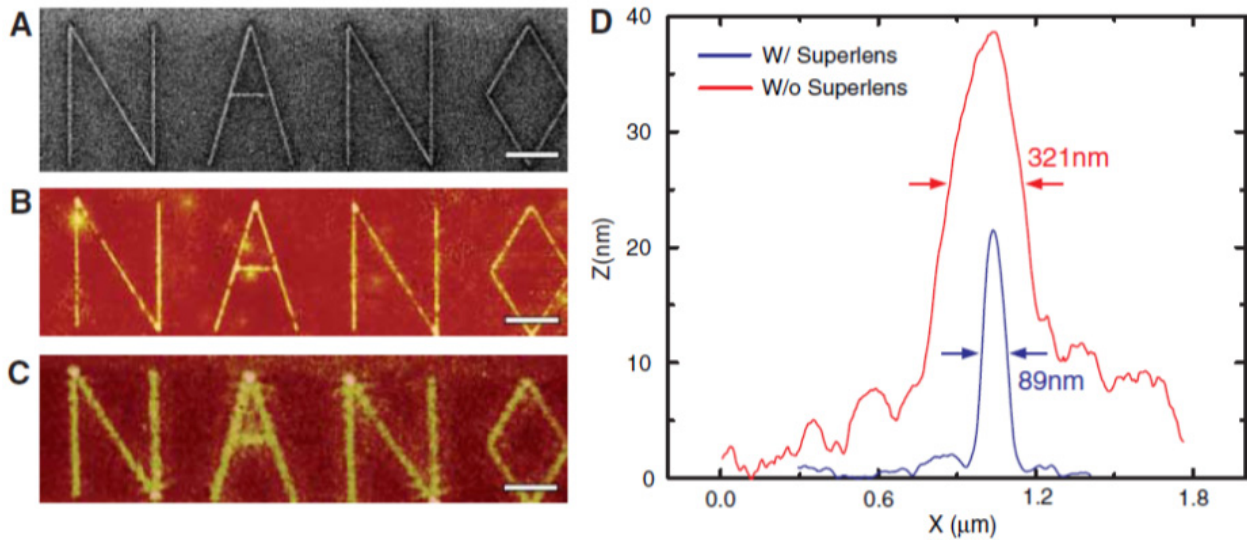


**Figure 3.** An arbitrary object "NANO" was imaged by silver superlens. (A) FIB image of the object. The linewidth of the "NANO" object was 40 nm. Scale bar in (A) to (C), 2 μm. (B) AFM of the developed image on photoresist with a silver superlens. (C) AFM of the developed image on photoresist when the 35 nm thick layer of silver was replaced by PMMA spacer as a control experiment. (D) The average cross section of letter "A" shows an exposed line width of 89 nm (blue line), whereas in the control experiment, we measured a diffraction-limited full width at half-maximum line width of  $321 \pm 10$  nm (red line). Reprinted with permission from "N. Fang, H. Lee, C. Sun and X. Zhang, *Science* 308, 534-537 (2005)." of copyright ©2005 American Institute of Physics.

## 2.2. Hyperlens

The images imaged by the superlens we talked about above are the same size as the objects. And there is no working distance. The hyperlens here was also proposed by Zhang's group [22]. It can magnify a sub-diffraction-limited image and projects it into the far field. Figure 4 A is the schematic of the hyperlens. It consists of a curved periodic stack of Ag (35 nm) and  $\text{Al}_2\text{O}_3$  (35 nm) deposited on a half-cylindrical cavity fabricated on a quartz substrate. Sub-diffraction-limited objects were inscribed into a 50-nm-thick chrome layer located at the inner surface (air side). The anisotropic metamaterial was designed so that the radial and tangential permittivities have different signs.



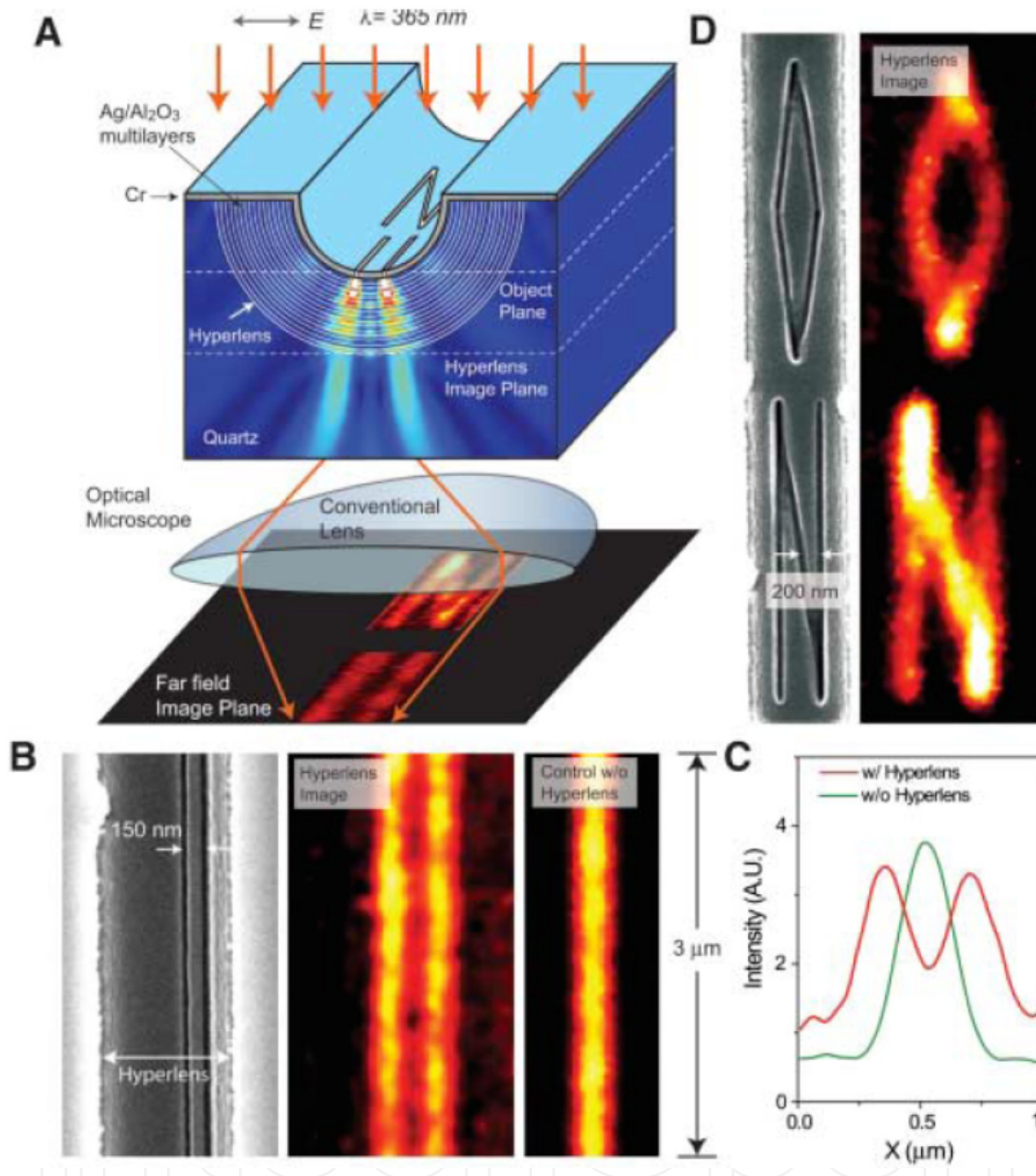


**Figure 4.** Optical hyperlens. (A) Schematic of heperlens and nymerical simulation of imaging of sub-diffraction-limited objects. (B) Hyperlens imaging of line pair object with line width of 35 nm and spacing of 150 nm. From left to right, scanning electron microscope image of the line pair object fabricated near the inner side of the hyperlens, magnified hyperlens image showing that the 150-nm-spaced line pair object can be clearly resolved, and the resulting diffraction-limited image from a control experiment without the hyperlens. (C) The averaged cross section of hyperlens image of the line pair object with 150-nm spacing (red), whereas a diffraction-limited image obtained in the control experiment (green). A.U.: arbitrary units. (D) An arbitrary object "ON" imaged with subdiffraction resolution. Line width of the object is about 40 nm. The hyperlens is made of 16 layers of Ag/Al<sub>2</sub>O<sub>3</sub>. Reprinted with permission from "Zhaowei Liu, Hyesog Lee, Yi Xiong, Cheng Sun, Xiang Zhang, Science 315. 1686 (2007)" of copyright ©2007 of AAAS.

The object imaged with hyperlens was a pair of 35-nm-wide lines spaced 150 nm apart. Upon illumination, the scattered evanescent field from the object enters the anisotropic medium and propagates along the radial direction. Because of the conservation of angular momentum, the tangential wave vectors are progressively compressed as the waves travel outward, resulting in a magnified image at the outer boundary of the hyperlens. Hence the magnified image (350-nm spacing) can be clearly resolved with an optical microscopy.

### 3. Plasmonic lens on the basis of subwavelength metallic structures

#### 3.1. Subwavelength metallic structure for superfocusing

##### 3.1.1. One-dimensional structures for focusing

In this section, we presented two types of tuning methods for the purpose of phase modulation: depth tuning [23] and width tuning [24-26] approaches.

##### 3.1.1.1. Depth-tuned. strctures

Three types of plasmonic slits (convex, concave, and flat/constant groove depth) with different stepped grooves have been designed and fabricated to achieve efficient plasmonic focusing and focal depth modulation of the transmitted beam. Figure 5 shows the fabricated depth-tuned plasmonic lens using focused ion beam milling [27]. The general design of the plasmonic slit is shown in Fig. 6 (a) [28]. When a TM polarized (magnetic field parallel to the y-direction) monochromatic plane wave impinges on the slit, it excites collective oscillations of the electrons at the surface, which is known as SPPs. The SPPs propagate along the surface of the metal film and are diffracted to the far-field by the periodic grooves, which are designed with a width smaller than half of the incident wavelength to allow a high diffraction efficiency [29]. Constructing interference of such diffracted beams leads to the focusing effect at a certain point on the beam axis [30]. Since the diffracted beams are modulated by the nanometric grooves, through adjusting the parameters of the grooves (such as our width, depth, period and number), the diffracted beams can be fully manipulated resulting in a tailored ultra-compact lens with subwavelength resolution and nanometer accuracy [31]. Most interestingly, it has been numerically found [32] that the relative phase at the exit end of the slit increases steadily with the increasing groove depth, making it possible to achieve continuous phase retardation by simply designing surrounding grooves with stepped depths as shown in Figs. 6 (b) and 6 (c). This has led to a great simplification of the plasmonic lens design without increasing the groove number or generating a bump on the metal film [33].

Figure 7 (a) presents a detailed comparison of the measured intensity distribution with simulation using FDTD at the slit cross section (along x-direction, as indicated by the white dot line in Fig. 2 (a) [23]). A good agreement has been found between the experiment and the theoretical prediction except that the measured full-width at a half-maximum (FWHM) of the central lobe (approximately 281 nm) is slightly larger than the calculated value of about 230 nm. This is because the measured intensity distribution approximately equals to the convolution of the finite probe size (30-80nm) and the actual intensity distribution of the transmitted light.

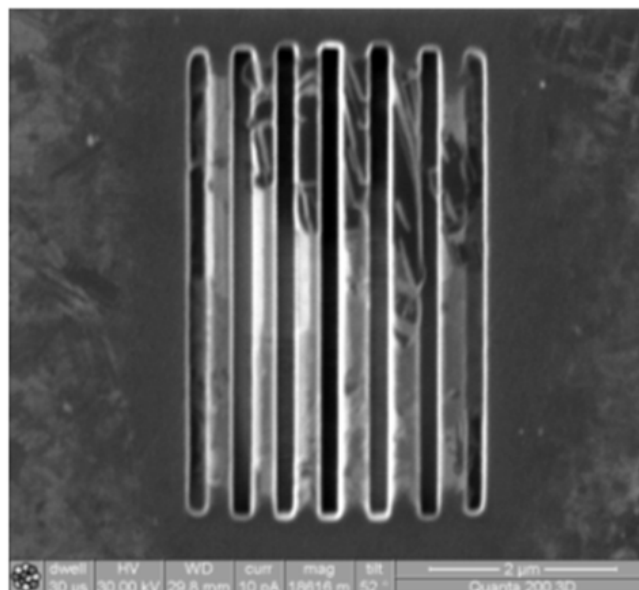


**Figure 5.** FIB image of the fabricated depth-tuned nanostructure (type of concave) on the Ag thin film with thickness of 200 nm.

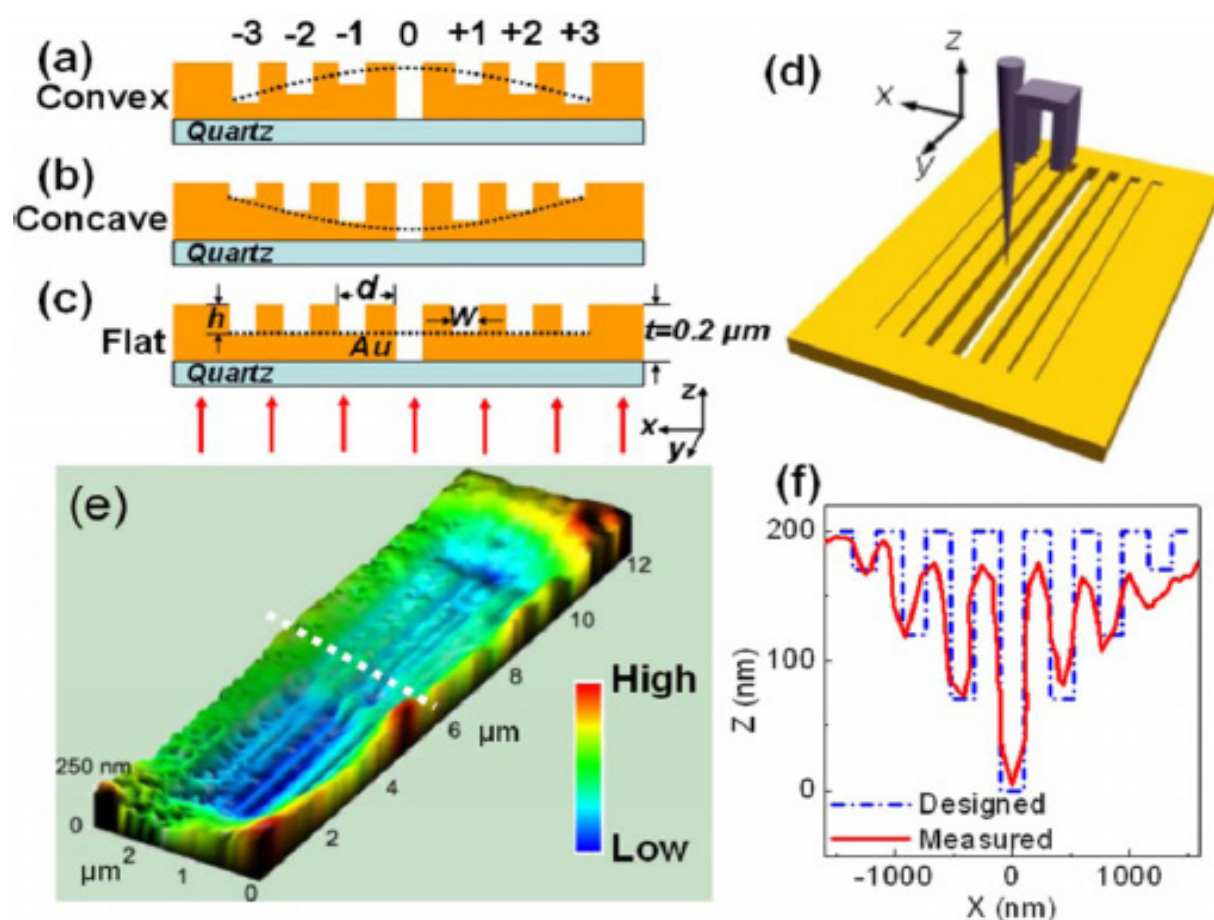


**Figure 6.** Schematic drawing of the nanoplasmonic slits with (a) convex, (b) concave and (c) flat shaped profiles. (d) Schematic drawing of near-field measurement setup. (e) Measured topographic image of the slit with concave corrugations. The marked area 'A' shows a larger overall depth than that of the area 'B'. (f) Cross section of the concave groove-slit at the position indicated by the dashed line in (e).



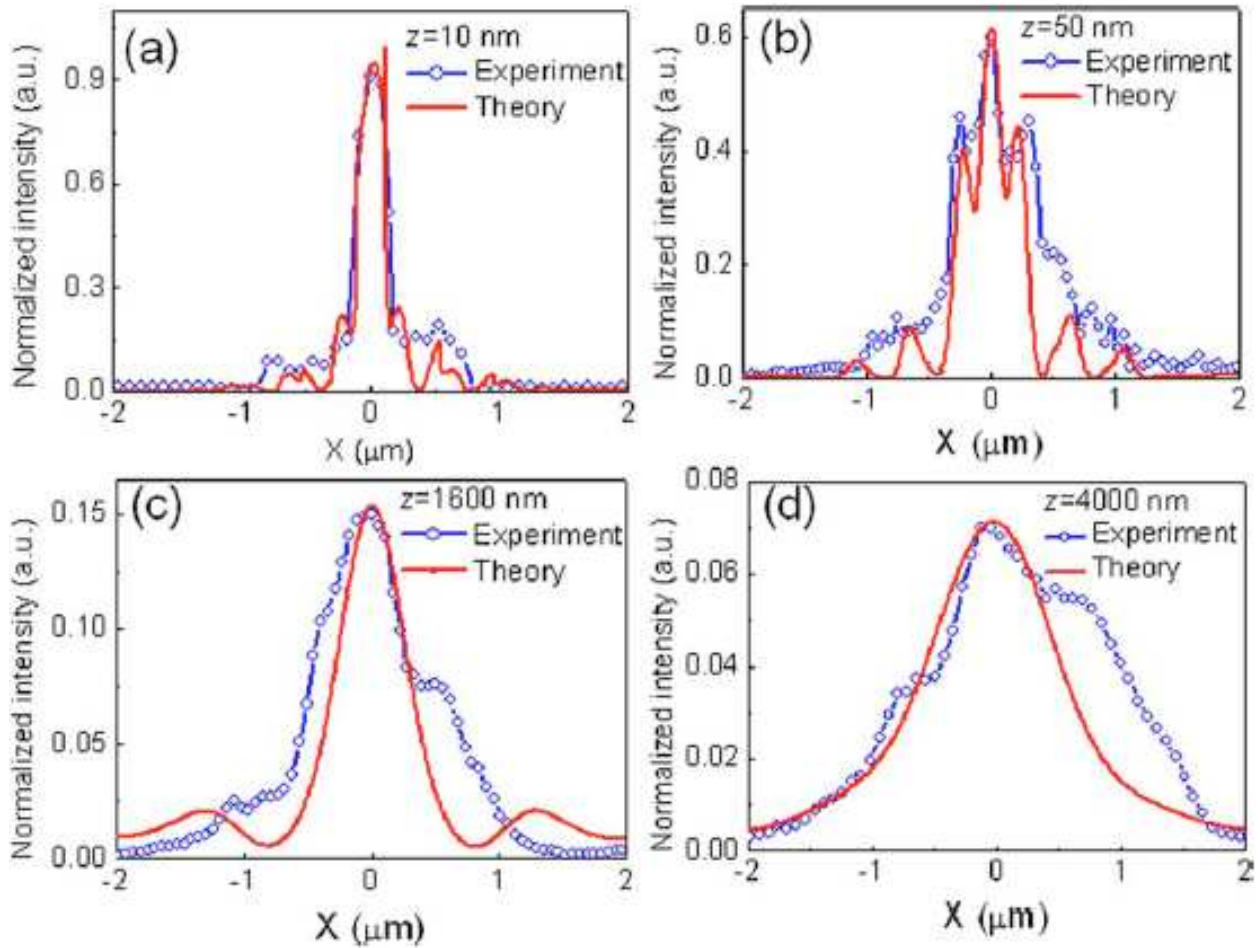


**Figure 7.** Comparison of measured and theoretical cross sections at  $x=0$  in Fig. 2 of the reference paper for (a)  $z=10$  nm, (b)  $z=50$  nm (c)  $z=1600$  nm and (d)  $z=4000$  nm.

Near-field measurement reveals unambiguously the light interaction with the slits and confirms the functionalities of the nanoplasmonic lens. The simple plasmonic lens demonstrated in this paper can find broad applications in ultra-compact photonic chips particularly for biosensing and high-resolution imaging. Among the three types metallic structures, the type of convave structure has best focusing performance.

In addition, V-shaped influence on focusing performance was analyzed in fabrication point of view [34]. The incident angle dependance on the focusing properties was discussed also in Ref. [35].

Regarding fabrication of the metallic structures with depth-tuned grooves, it is worthy to point out that the geometrical characterization issue using atomic force microscope after focused ion beam direct milling [31]. Large measurement error is found during geometrical characterization of the nanostructures by use of an atomic force microscope (AFM) working in tapping mode. Apex wearing and  $34^\circ$  full cone angle of the probe generate the measurement errors during characterizing the nanostructures with the feature size of 200 nm and below. To solve this problem, a FIB trimmed AFM probe is employed in the geometrical characterization, as shown in Fig. 8. The results show that the error is improved greatly using the trimmed probe.

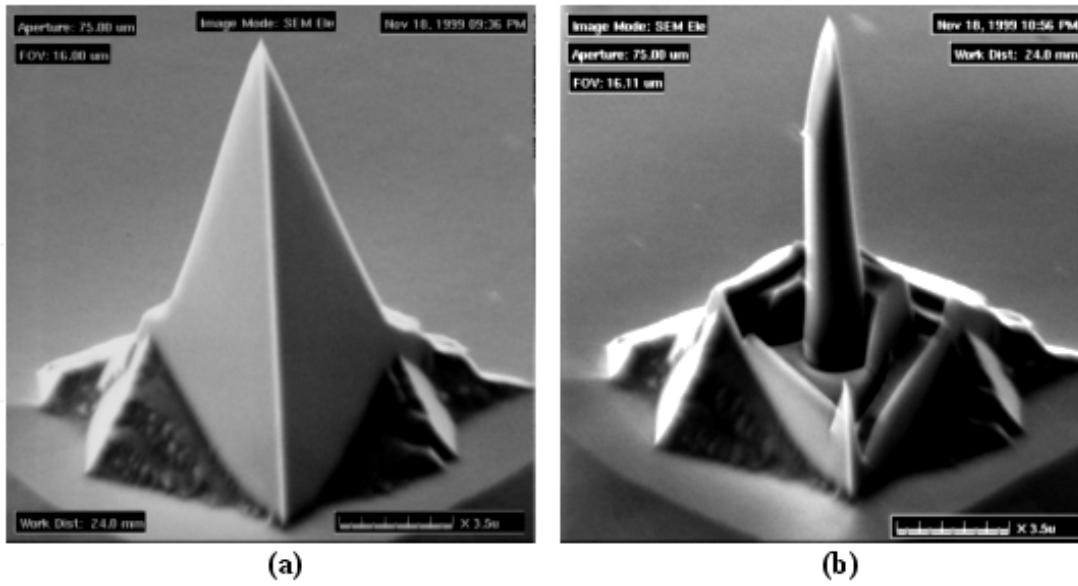


**Figure 8.** AFM probe for tapping mode. (a) the commercial probe with half cone angle of  $17^\circ$  and material of  $\text{Si}_3\text{N}_4$ . (b) the FIB trimmed probe with high aspect ratio.

Influence of polarization states on focusing properties of the depth-tuned metallic structures was reported [31]. The structure was designed with geometrical parameters shown as Fig. 9. Figure 10 shows the total electric-field intensity  $|E|^2 = |E_x|^2 + |E_y|^2 + |E_z|^2$  at x-y plane along the longitudinal direction at  $z = 1.35 \mu\text{m}$  at  $\lambda = 420 \text{ nm}$  for the (a) elliptical polarization (EP), (b) circular polarization (CP), and (c) radial polarization (RP) cases. The intensity of transverse electric field,  $|E_x|^2 + |E_y|^2$ , is significantly tuned. In the figure, the intensity along the horizontal (x) is equal to that along the vertical (y), while the intensity along the

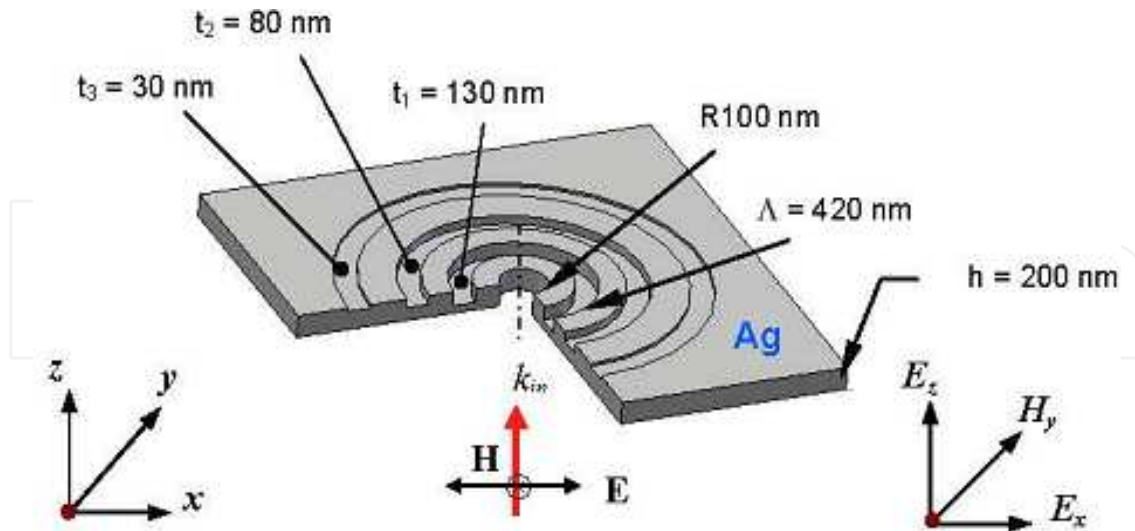


**Figure 9.** An annular plasmonic lens having a depth-tuned structure (groove depths,  $t_1 = 130 \text{ nm}$ ,  $t_2 = 80 \text{ nm}$  and  $t_3 = 30 \text{ nm}$ ) milled in the output side of a Ag thin film (thickness,  $h = 200 \text{ nm}$ ). Other structure parameters are: central hole diameter =  $200 \text{ nm}$ , groove width =  $200 \text{ nm}$ , and groove period =  $420 \text{ nm}$ . The structure is incident with TM-polarized light having electric vector along the x direction. Reprinted with permission from “Jun Wang, Wei Zhou and Anand K. Asundi, Opt. Express 17, 8137-8143 (2009).” of copyright ©2009 Optical Society of American.

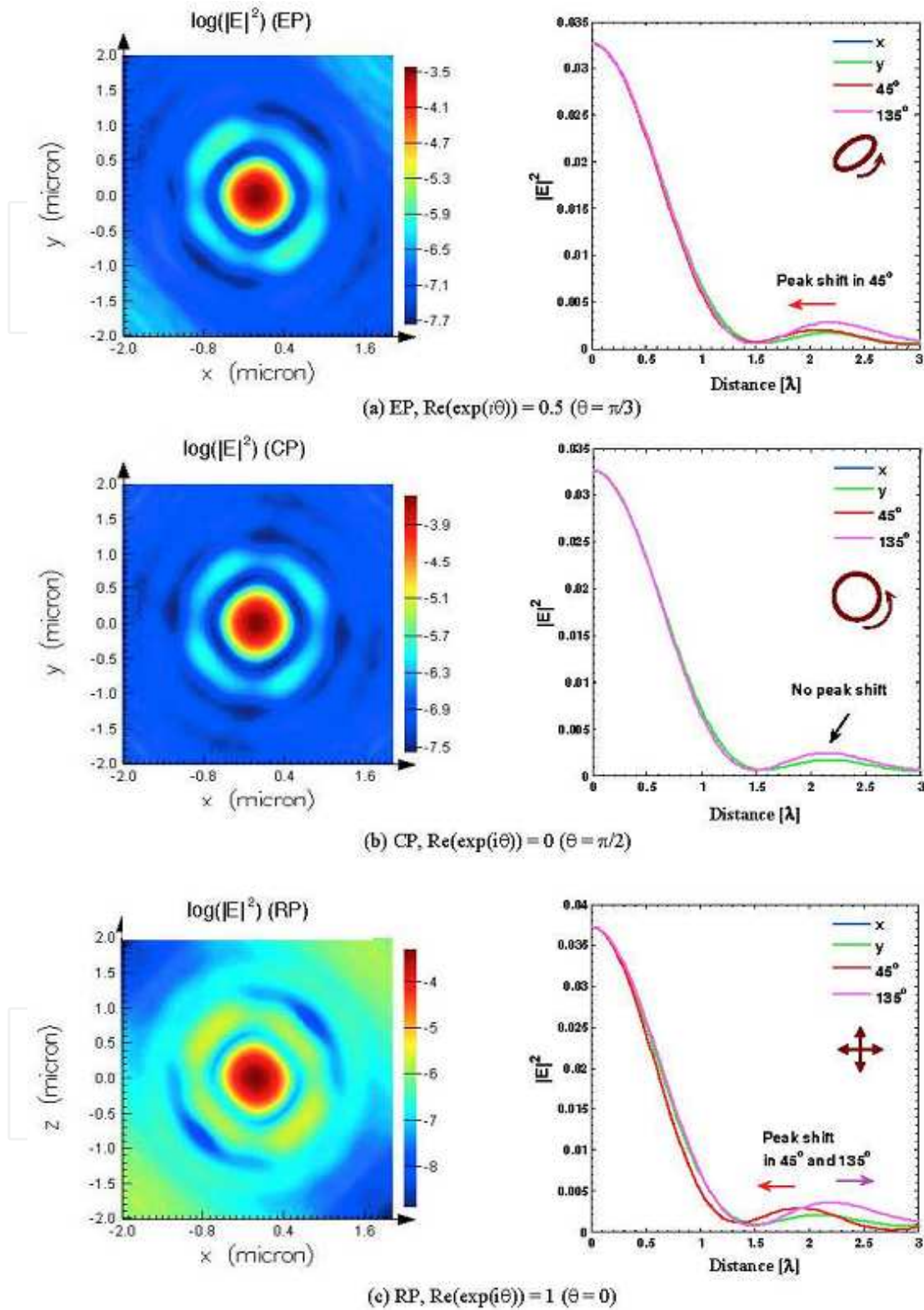


**Figure 10.** Total electric field (left) transmitted through the structure under illumination using different polarization states, including (a) CP, (b) EP, and (c) RP, showing the phase modulation effect on the beam profile (right) along the transverse direction in  $x$  and  $y$  and diagonal directions along  $45^\circ$  and  $135^\circ$  with respect to the  $x$ . Refer to Fig. 1 for the directions. Reprinted with permission from "Jun Wang, Wei Zhou and Anand K. Asundi, Opt. Express 17, 8137-8143 (2009)." of copyright ©2009 Optical Society of American.

diagonal directions ( $45^\circ$  and  $135^\circ$  with respect to the  $x$  is tuned), the peak shift is observed at the side lobe, which is  $<0.1\lambda$  for the EP case. In Fig. 10 (a), in the direction of  $45^\circ$ . And the beam in  $45^\circ$  is narrower than that in the  $x$ - or  $y$ -directions. In addition, the phase function  $\text{Re}(\exp(i\theta))$  indicates tuning capability.  $\text{Re}(\exp(i\theta)) = 0.5$ , where  $\theta = \pi/3$ , for the EP case, and the phase function becomes 0 for the CP and 1 for the RP case. For example, in Fig. 10 (b), the uniformly distributed total-electric-field intensity is observed in the  $x$ - $y$  plane, while, in Fig. 10 (c), the peak shifts  $0.2\lambda$  in the  $45^\circ$  larger than that for the EP case, and much narrow beam is observed in the same direction. The same plasmonic modes are observed for CP, EP, or RP polarization cases as for TM case. Using a polarized plane wave the transverse electric field is tuned; the tuning  $45^\circ$  and  $135^\circ$  with respect to effect on focus spot is observed along the diagonal directions in  $45^\circ$  the  $x$ -direction. Of the cases, RP approach forms the smallest focus spot along the  $45^\circ$  using  $\text{Re}[\exp(i\theta)]=1$ , showing maximum tuning capability, while CP approach the phase function  $\text{Re}[\exp(i\theta)]=0$  forms a symmetrically electric field distribution in the focal plane. Phase function indicates the tuning capability.

#### 3.1.1.2. Width-tuned structures

A novel method is proposed to manipulate beam by modulating light phase through a metallic film with arrayed nano-slits, which have constant depth but variant widths. The slits transport electro-magnetic energy in the form of surface plasmon polaritons (SPPs) in nanometric waveguides and provide desired phase retardations of beam manipulating with variant phase propagation constant. Numerical simulation of an illustrative lens design example is performed through finite-difference time-domain (FDTD) method and shows agreement with theory analysis result. In addition, extraordinary optical transmission of SPPs through sub-wavelength metallic slits is observed in the simulation and helps to improve elements's energy using factor.

To illustrate the above idea of modulating phase, a metallic nano-slits lens is designed [24]. The parameters of the lens are as follows:  $D = 4 \mu\text{m}$ ,  $f = 0.6 \mu\text{m}$ ,  $\lambda = 0.65 \mu\text{m}$ ,  $d = 0.5 \mu\text{m}$ , where  $D$  is the diameter of the lens aperture,  $f$  the focus length, the wavelength and  $d$  the thickness of the film. The two sides of the lens is air. The schematic of lens is given in Fig. 11, where a metallic film is perforated with a great number of nano-slits with specifically designed widths and transmitted light from slits is modulated and converges in free space.

After numerous iterations of calculation using the FDTD algorithm, the resulting Poynting vector is obtained and showed in Fig. 12 (a). A clear-cut focus appears about 0.6 micron away from the exit surface, which agrees with our design. The cross section of focus spot in  $x$  direction is given in Fig. 12 (b), indicating a full-width at half-maximum (FWHM) of 270 nm. The extraordinary light transmission effects of SPPs through sub-wavelength slits is also observed in the simulation with a transmission enhance factor of about 1.8 times. These advantages promise this method to find various potential applications in nano-scale beam shaping, integrate optics, data storage, and near-field imaging ect.



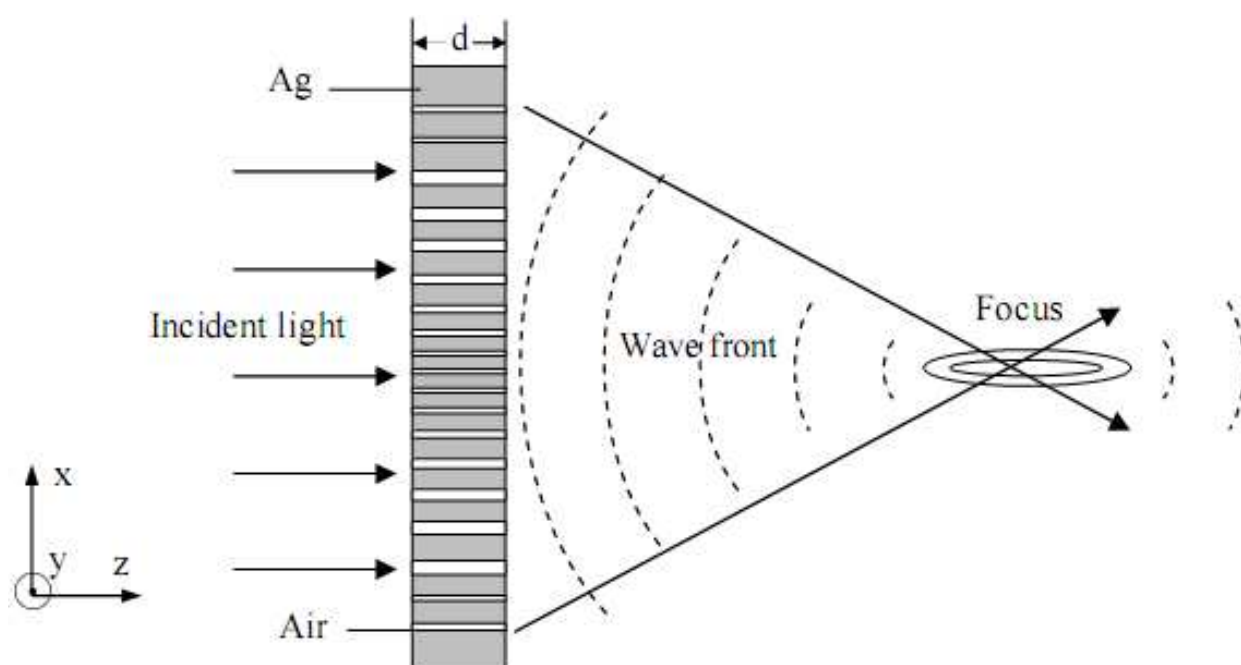


**Figure 11.** A schematic of a nano-slit array with different width formed on thin metallic film. Metal thickness in this configuration is  $d$ , and each slit width is determined for required phase distribution on the exit side, respectively. A TM-polarized plane wave (consists of  $E_x$ ,  $H_y$  and  $E_z$  field component, and  $H_y$  component parallel to the  $y$ -axis) is incident to the slit array from the left side. Reprinted with permission from “H. F. Shi, C. T. Wang, C. L. Du, X. G. Luo, X. C. Dong, and H. T. Gao, *Opt. Express* 13, 6815-6820 (2005).” of copyright ©2009 Optical Society of American.

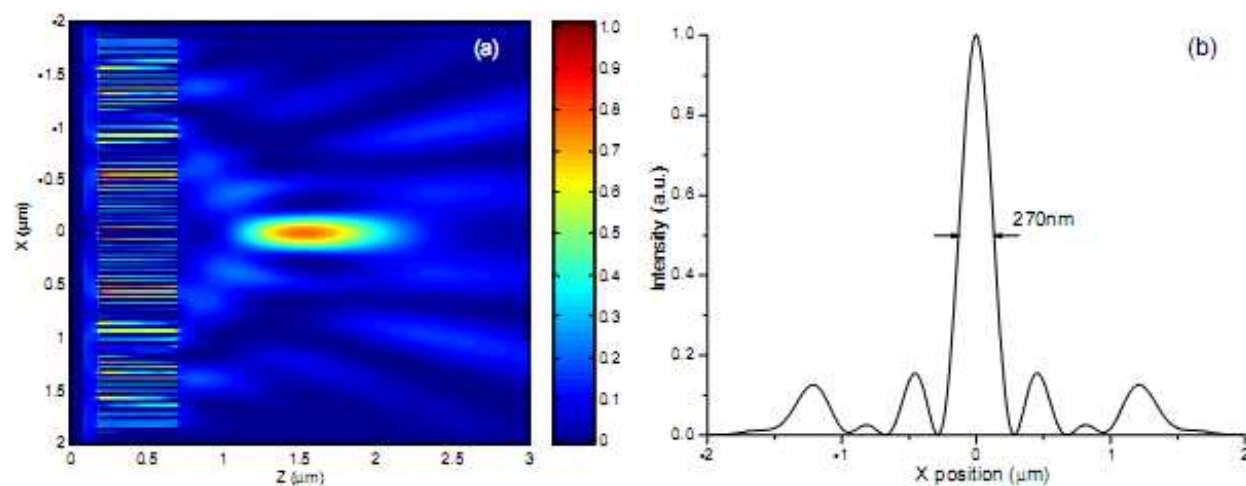


**Figure 12.** (a) FDTD calculated result of normalized Poynting Vector  $S_z$  for designed metallic nano-slits lens. Film thickness is 500nm, and the total slits number is 65. The structure's exit side is posited at  $z=0.7 \mu\text{m}$ . (b) Cross m.section of the focus at  $z=1.5 \mu\text{m}$ . Reprinted with permission from “H. F. Shi, C. T. Wang, C. L. Du, X. G. Luo, X. C. Dong, and H. T. Gao, *Opt. Express* 13, 6815-6820 (2005).” of copyright ©2009 Optical Society of American.

As an experimental verification example, Lieven et. al. [37] experimentally demonstrated planar lenses based on nanoscale slit arrays in a metallic film. The lens structures consist of optically thick gold films with micron-size arrays of closely spaced, nanoscale slits of varying

widths milled using a focused ion beam. They found an excellent agreement between electromagnetic simulations of the design and confocal measurements on manufactured structures. They provide guidelines for lens design and show how actual lens behavior deviates from simple theory.

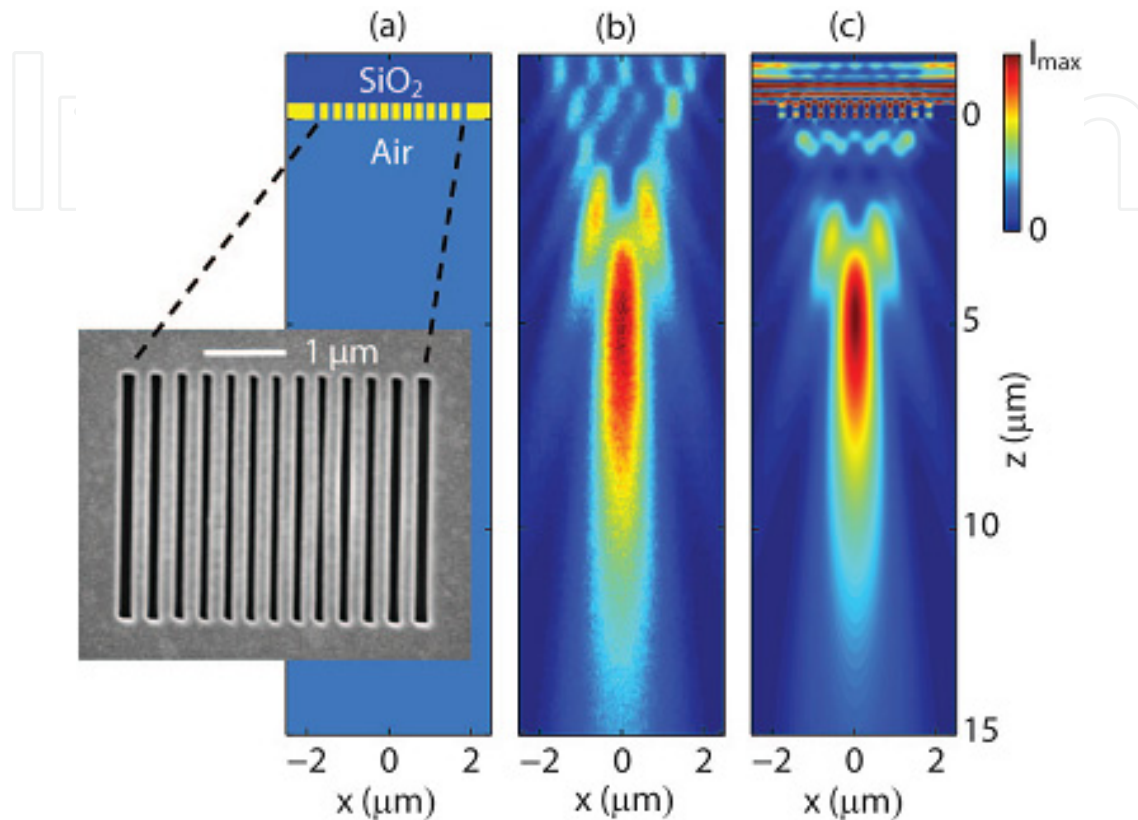


**Figure 13.** Planar lens based on nanoscale slit array in metallic film. (a) Geometry of the lens consisting of a 400nm optically thick gold film (yellow) with air slits of different widths (80 to 150 nm) (light blue) milled therein on a fused silica substrate (dark blue). The inset shows a scanning electron micrograph of the structure as viewed from the air-side. (b) Focusing pattern measured by confocal scanning optical microscopy (CSOM). (c) Finite-difference and frequency-domain (FDFD) simulated focusing pattern of the field intensity through the center of the slits. In order to show the features of the focus spot clearly, the field intensity inside the slits is saturated. Reprinted with permission from “LievenVerslegers et. al., Nano Lett. 9, 235-238 (2009)” of copyright ©2009 Chemical Society of American.

The basic geometry consists of an array of nanoscale slits in an otherwise opaque metallic film (see Fig. 13 (a)). Figure 13 shows the main results of the work, which combines fabrication, characterization, and simulation. Panel (a) shows the fabricated structure, while panels (b) and (c) represent the measured and simulated field intensity in a cross section through the center of the slits (along the x-direction). Both the measurement and the simulation clearly demonstrate focusing of the wave. The agreement between experiment and simulation is excellent. Moreover, the simulation image is generated using the designed parameters as the slit width rather than the actual slit width measured in the SEM, as is commonly done when comparing nanophotonics simulation and experiments. The agreement there thus indicates the robustness in design and the fault tolerance of this

approach for focusing. The effect of lens size can be exploited to control the focusing behavior as is shown clearly in Fig. 14. Both lenses introduce the same curvature to the incident plane wave as the lens from Fig. 13, since we consist of slits with the same width as the original design ( $2.5\ \mu\text{m}$  long). By omitting one outer slit on each side for the lens in Fig. 14 (a), one gets the lens, as shown in Fig. 14 (b).

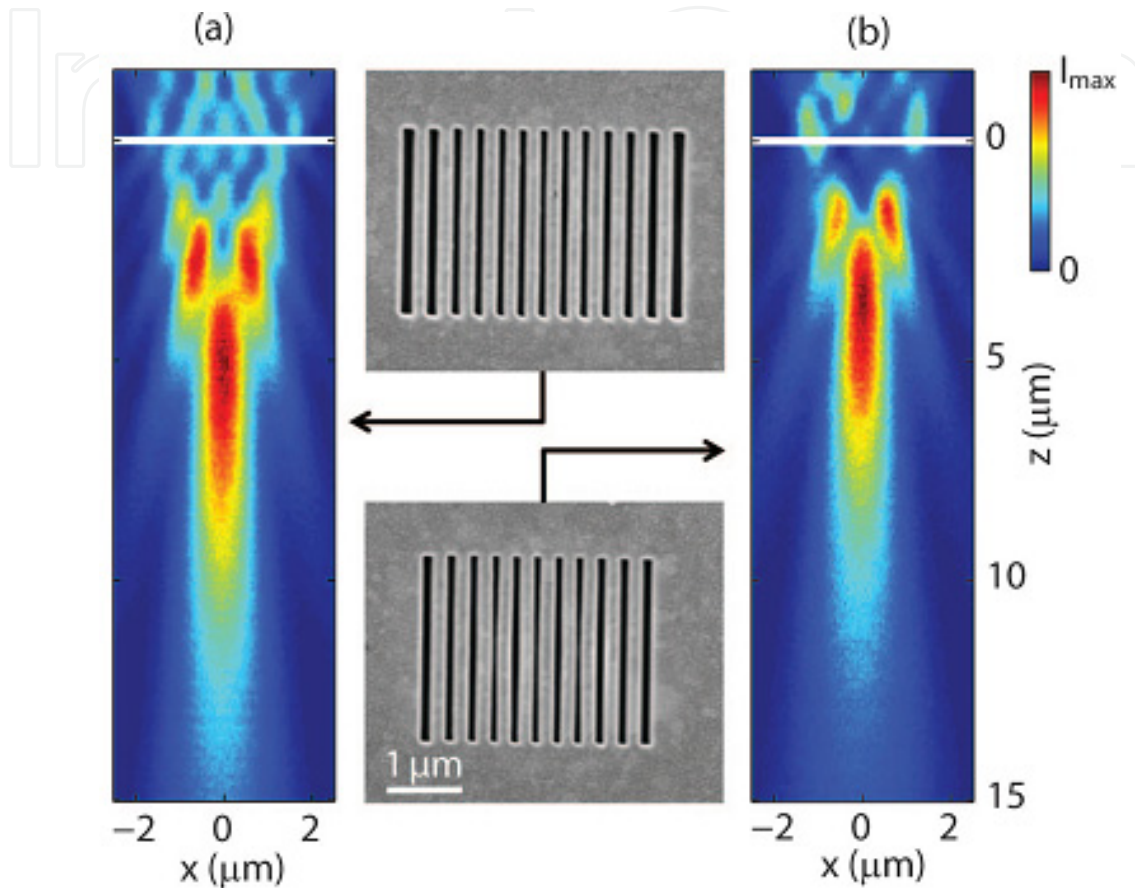


**Figure 14.** Control of the cylindrical lens behavior by design of nanoscale slit array parameters. Effect of lens size on focusing for (a) a lens with 13 slits ( $80\text{-}150\text{nm}$  by  $2.5\ \mu\text{m}$ ) and (b) a lens with 11 slits ( $80\text{-}120\text{nm}$  by  $2.5\ \mu\text{m}$ ). The white line gives an estimate of the lens position. Both scanning electron micrographs are on the same scale. Reprinted with permission from “LievenVerslegers et. al., Nano Lett. 9, 235-238 (2009)” of copyright ©2009 Chemical Society of American.

This first experimental demonstration is a crucial step in the realization of this potentially important technology for many applications in optoelectronics. Moreover, the design principles presented here for the special case of a lens can be applied to construct a wide range of optical components that rely on tailoring of the optical phase front.

### 3.1.2. Two-dimensional structures for focusing

#### 3.1.2.1. Circular grating-based metallic structures for focusing

Recently, Jennifer et. al. reported the generation and focusing of surface plasmon polariton (SPP) waves from normally incident light on a planar circular grating (constant slits width

and period) milled into a silver film [38]. The focusing mechanism is explained by using a simple coherent interference model of SPP generation on the circular grating by the incident field. Experimental results concur well with theoretical predictions and highlight the requirement for the phase matching of SPP sources in the grating to achieve the maximum enhancement of the SPP wave at the focal point. NSOM measurements show that the plasmonic lens achieves more than a 10-fold intensity enhancement over the intensity of a single ring of the in-plane field components at the focus when the grating design is tuned to the SPP wavelength.

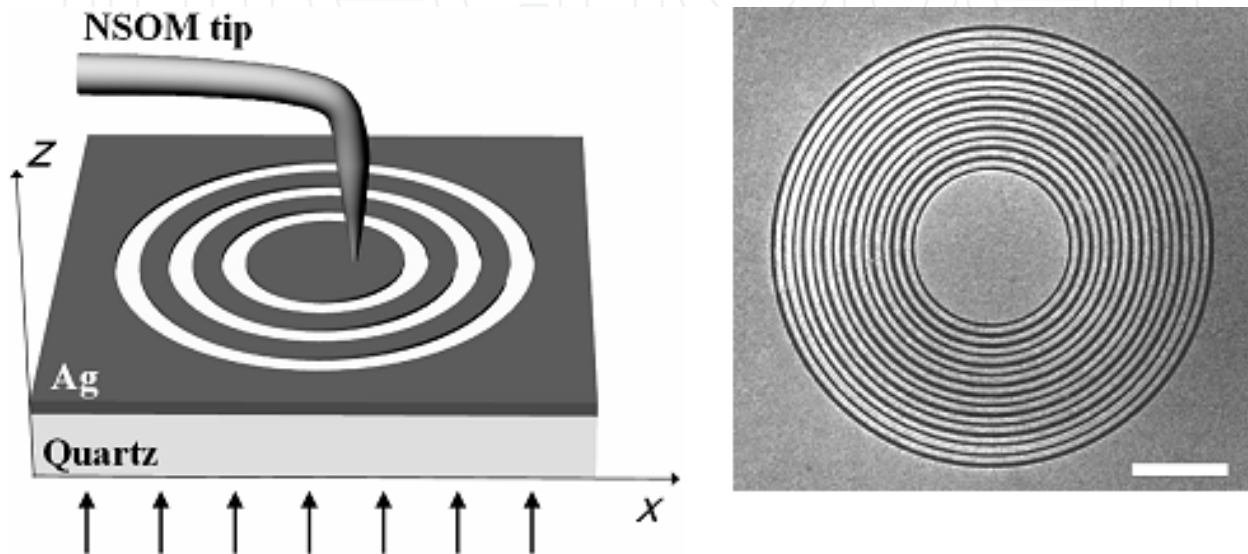


**Figure 15.** (a) Experimental scheme for near-field measurements. Circular gratings are cut into a silver film deposited on a quartz substrate. Laser light is normally incident from the quartz side, and the electromagnetic near-field is monitored with a metal coated NSOM tip. (b) SEM image of a sample with 15 rings. The scale bar is 5 microns. Reprinted with permission from “Jennifer M. Steele, Zhaowei Liu, Yuan Wang, and Xiang Zhang, *Opt. Express* 14, 5664-5670 (2006).” of copyright ©2006 Optical Society of American.

To investigate this focusing experimentally, rings with different periods were cut into 150 nm thick silver films. Silver was evaporated onto a quartz plate at a high rate to ensure a surface with minimal roughness. Rings were milled into the metal using an FEI Strata 201 XP focused ion beam (FIB), with the inner most ring having a diameter of 8 microns. Additional rings were added with a period either close to or far from resonance with the excited SPP waves. The surface plasmons were excited with linearly polarized laser light incident from the quartz side. The electromagnetic near-field of these structures was recorded using near-field scanning optical microscopy (NSOM) in collection mode using a metal coated NSOM tip. A metal coated tip was chosen over an uncoated tip to increase the resolution of the scan. Previous experimental results on samples with similar geometry compare favorably with computer simulations, indicating the interaction of the SPP near field with the metal tip is negligible. The measurement scheme can be seen in Fig. 15 (a) with an SEM image of a typical sample shown in Fig. 15 (b). The phase change of SPP waves across a barrier is an interesting issue that has received very little attention. If the slit width



is much smaller than the SPP wavelength, the slit will have very little effect on the SPP and the phase change should be very small. However, if the slit width is on the order of the SPP wavelength, as the SPP waves cross a slit opposite charges will be induced on opposite sides of the slit, providing quasi-electrostatic coupling across the barrier. The authors claimed that it is possible that the phase change will be sensitive to the slit width. The number and period of rings, film material, and slit geometries provide experimental handles to tune the plasmonic lens to accommodate specific applications, making this technique a flexible plasmonic tool for sensing applications.

The following two sections below introduce the metallic subwavelength structures with chirped (variant periods) slits and nanopinhole acted as the plasmonic lenses for the purpose of superfocusing.

### 3.1.2.2. Illumination under linear polarization state

A novel structure called plasmonic micro-zone plate-like (PMZP) or plasmonic lens with chirped slits is put forth to realize superfocusing. It was proposed by Fu's group [39,40]. Unlike conventional Fresnel zone plate (CFZP), a plasmonic structure was used and combined with a CFZP. Configuration of the PMZP is an asymmetric structure with variant periods in which a thin film of Ag is sandwiched between air and glass. The PMZP is a device that a quartz substrate coated with Ag thin film which is embedded with a zone plate structure with the zone number  $N < 10$ . Figure 16 is an example of schematic diagram of the structure.

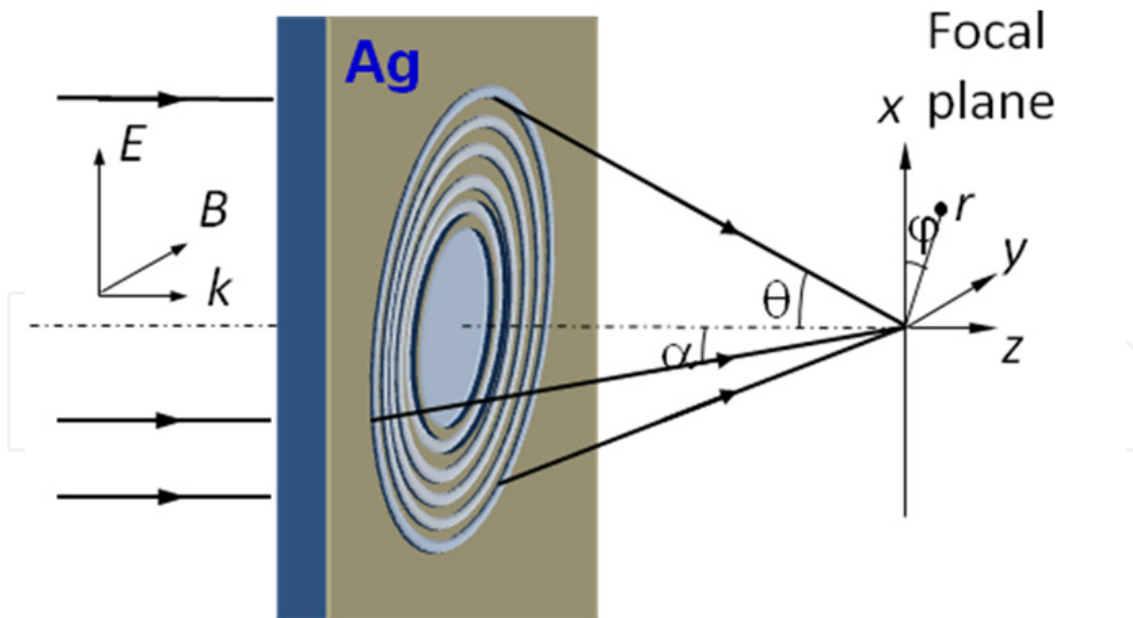


**Figure 16.** Schematic of the plasmonic micro-zone plate for super-focusing.

Following the electromagnetic focusing theory of Richard and Wolf (Richards & Wolf, 1959)[41], the electric field vector in the focal region is given by,

$$\mathbf{E}(r, z, \varphi) = -i [I_0(r, z) + I_2(r, z) \cos 2\varphi] \mathbf{i} - i I_2(r, z) \sin 2\varphi \mathbf{j} - 2I_1(r, z) \cos \varphi \mathbf{k}. \quad (2)$$

Let  $\mathbf{i}$ ,  $\mathbf{j}$ ,  $\mathbf{k}$  be the unit vectors in the direction of the co-ordinate axes. To be integral over the individual zones,  $I_0$ ,  $I_1$ ,  $I_2$  are expressed as,

$$I_0(r, z) = \sum_n T_n \int_{\alpha_{n-1}}^{\alpha_n} \sqrt{\cos \theta} (1 + \cos \theta) J_0(kr \sin \theta) \exp(ikz \cos \theta) \sin \theta d\theta,$$

$$I_1(r, z) = \sum_n T_n \int_{\alpha_{n-1}}^{\alpha_n} \sqrt{\cos \theta} \sin \theta J_1(kr \sin \theta) \exp(ikz \cos \theta) \sin \theta d\theta,$$

$$I_2(r, z) = \sum_n T_n \int_{\alpha_{n-1}}^{\alpha_n} \sqrt{\cos \theta} (1 - \cos \theta) J_2(kr \sin \theta) \exp(ikz \cos \theta) \sin \theta d\theta.$$

The wave vector  $k = 2\pi/\lambda$ .

According to the equation, the intensity of lateral electric field component,  $|E_x|^2$ , follows the zero-order Bessel function  $J_0$  of the first kind, while the intensity of longitudinal electric field component,  $|E_z|^2$ , follows the first-order Bessel function  $J_1$  of the first kind. In the total electric field intensity distribution, all the field components add up. With high numerical aperture, this leads to not only asymmetry of the focus spot but also an enlarged focus spot. As shown in Figs. 17 (a)~(b), the total electric field and individual electric field components,  $|E|^2$ ,  $|E_x|^2$ , &  $|E_z|^2$ , emerged from  $\lambda_{sp}$ -launched FZP lens are in comparison with that the total electric field and individual electric field components from a  $\lambda_{in}$ -launched PMZP lens. It is found that the intensity ratio,  $|E_x|^2/|E_z|^2$ , can increase up to 10 times for the  $\lambda_{sp}$ -launched PMZP lens. A focus spot having the polarization direction along the  $x$  direction is obtained.

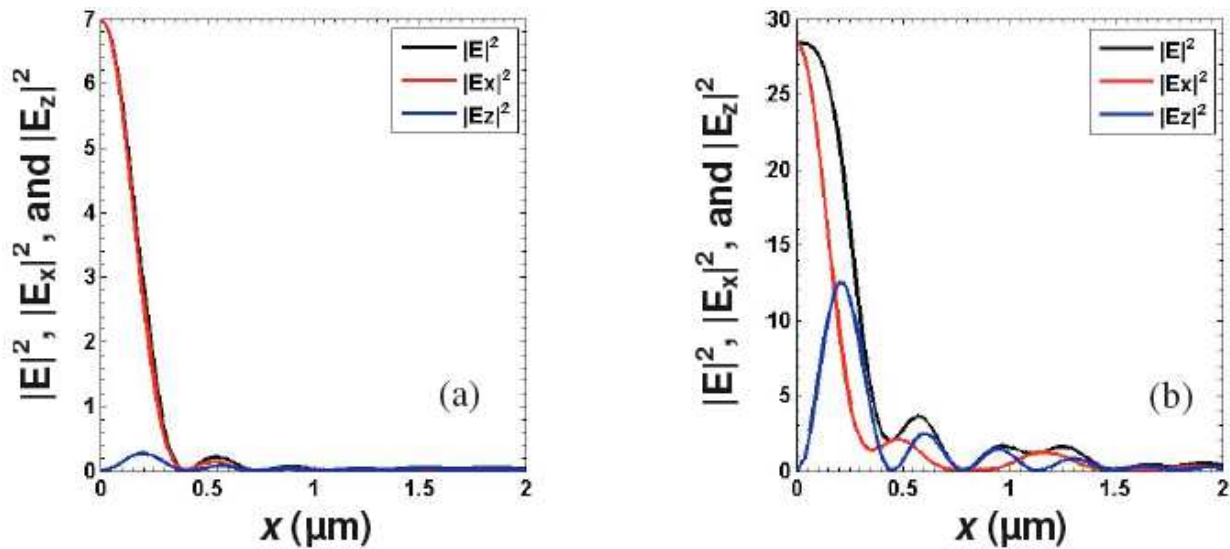


**Figure 17.** The total electric field and electric field components,  $|E|^2$ ,  $|E_x|^2$ , and  $|E_z|^2$ , emerged from (a) a  $\lambda_{sp}$ -launched FZP lens and (b) a  $\lambda_{in}$ -launched FZP lens. It is observed that the proposed superlens enables to restrict the depolarization effect and produces a linearly- polarized focus spot having the polarization direction in the  $x$  direction.

The chirped slits can form a focal region in free space after the exit plane. The final intensity at the focal point is synthesized by iteration of each zone focusing and interference each other, and can be expressed as

$$I = \alpha \sum_{i=1}^N C I_0 \frac{4r_i}{\lambda_{SP}} e^{-(r_i / l_{SP})} \quad (3)$$

where  $I_0$  is the incident intensity,  $r_i$  is the inner radius of each zone,  $i$  is the number of the zones,  $l_{SP}$  is the propagation length for the SPP wave,  $\alpha$  is interference factor, and  $C$  is the coupling efficiency of the slits.  $C$  is a complicated function of the slit geometry and will likely have a different functional form when the slit width is much larger or much smaller than the incident wavelength

The PMZPs is an asymmetric structure. For an evanescent wave with given  $k_x$ , we have  $k_{zj} = +[\epsilon_j(\omega/c)^2 - k_x^2]^{1/2}$  for  $j=1$  (air) and  $j=3$  (glass) and  $k_{zj} = +i[k_x^2 - \epsilon_j(\omega/c)^2]^{1/2}$  for  $j=2$  (Ag film). Superfocusing requires regenerating the evanescent waves. Thus the PMZP needs to be operated with the condition  $|k_{z1}/\epsilon_1 + k_{z2}/\epsilon_2| |k_{z2}/\epsilon_2 + k_{z3}/\epsilon_3| \rightarrow 0$ . Physically, this would require exciting a surface plasmon at either the air or the glass side. For  $E_\perp$  wave, a negative permittivity is sufficient for focusing evanescent waves if the metal film thickness and object are much smaller than the incident wavelength. Because electric permittivity  $\epsilon < 0$  occurs naturally in silver and other noble metals at visible wavelengths, a thin metallic film can act as an optical super lens. In the electrostatic limit, the p-polarized light, dependence on permeability  $\mu$  is eliminated and only permittivity  $\epsilon$  is relevant. In addition, diffraction and interference contribute to the transition from the evanescent waves to the propagation waves in the quasi-far-field region. Above all, the PMZPs form super focusing by interference of the localized SPP wave which is excited from the zones. This makes it possibly work at near and quasi-far-field with lateral resolution beyond diffraction limit. Also the PMZP has several zones only, its dimension is decreased greatly compared the CFZP.

As an example, an appropriate numerical computational analysis of a PMZP structure's electromagnetic field is carried out using finite-difference and time-domain (FDTD). It is illuminated by a plane wave with a 633 nm incident where Ag film has permittivity  $\epsilon_m = \epsilon'_m + i\epsilon''_m = -17.6235 + 0.4204i$ . An Ag film with thickness  $h_{Ag} = 300\text{nm}$  centered at  $z=150$  nm has an embedded micro-zone-plate structure. Zone number  $N=8$ , and outer diameter  $OD=11.93\text{ }\mu\text{m}$ . The widths of each zone from first ring to last ring, calculated by using the conventional zone plate equations, are 245, 155, 116, 93, 78, 67, 59, and 52 nm. In the FDTD simulations, the perfectly

matched layer boundary condition was applied at the grid boundaries. Figure 17 is the simulation result. From the result, the simulated focal length of the PMZP,  $f_{PMZP}$  and depth of focus (DOF) are larger than those of the designed values using the classical equations  $r_n = (n\lambda f_{FZP} + n^2\lambda^2/4)^{1/2}$  and  $DOF = \pm 2\Delta r^2/\lambda$ , where  $n=1, 2, 3, \dots$ ,  $f_{PMZP}$  is the designed principal focal length of Fresnel zone plates and given in terms of radius  $R$  of the inner ring

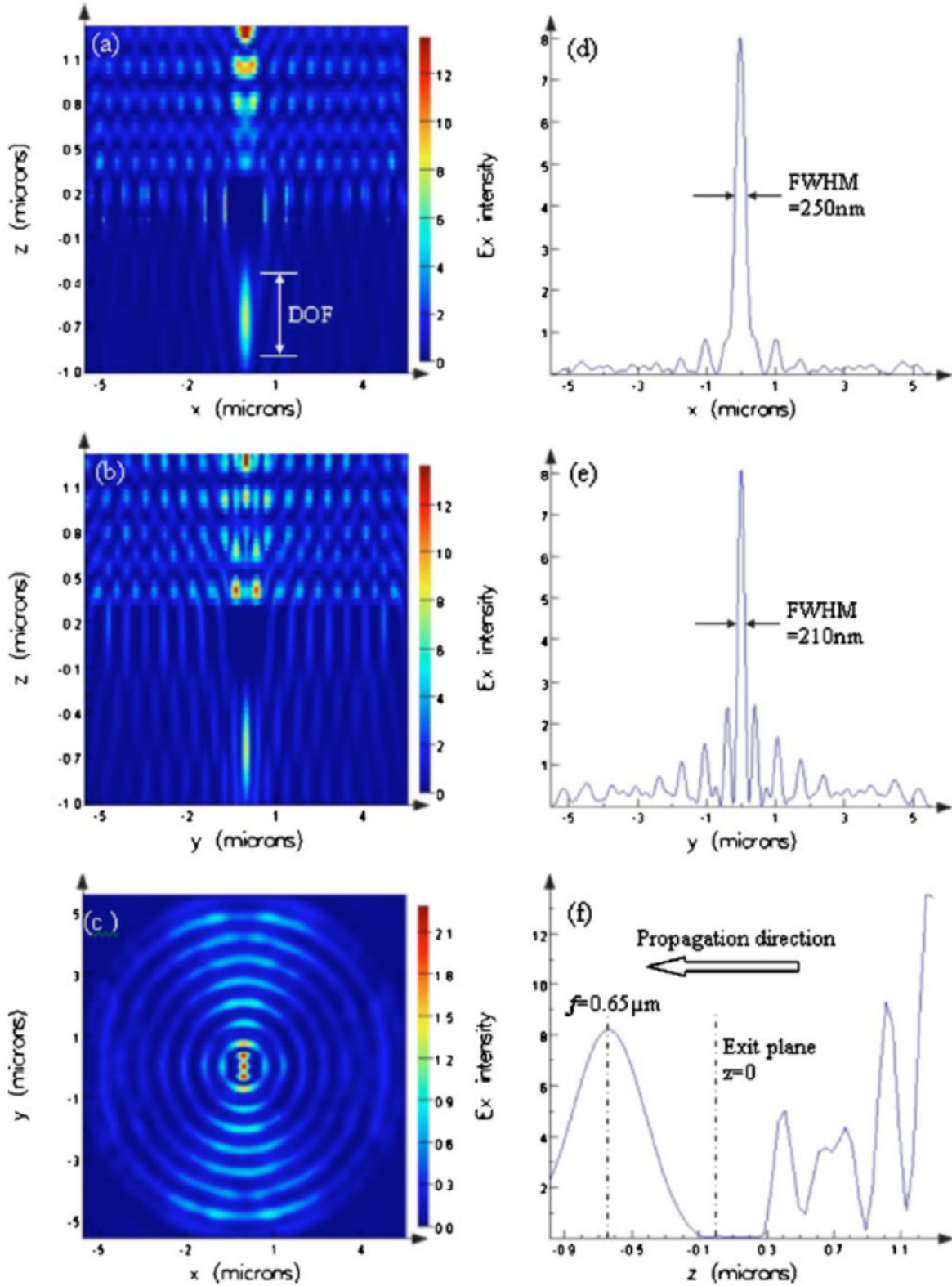


**Figure 18.** The simulation result of the example of the PMZP. The propagation direction is  $z$ . Electric field intensity  $|E_x|^2$  at (a)  $y$ - $z$  plane, (b)  $x$ - $z$  plane, and (c)  $x$ - $y$  plane. Electric field transmission in the line  $z = -0.65 \mu\text{m}$  (calculated focal plane) at (d)  $x$ - $z$  plane,  $y = 0$ ; (e)  $y$ - $z$  plane,  $x = 0$ ; and (f)  $y$ - $z$  plane,  $x = 0$ . The designed focal length and outmost zone width using scalar theory is  $f = 1 \mu\text{m}$  and  $53 \text{ nm}$ , respectively. The calculated DOF is  $\sim 700 \text{ nm}$  (scalar theory designed value is  $8.85 \text{ nm}$ ) the site  $z = 0$  is the exit plane of the Ag film.



and incident wavelength by  $f_{FZP} = R^2 / \lambda$ ,  $\Delta r$  is the outmost zone width, and  $\lambda$  is the incident wavelength. It may be attributed to the SPPs wave coupling through the cavity mode and is involved for the contribution of the beam focusing. The focusing is formed by interference between the SPPs wave and the diffraction waves from the zones.

Figures 18 (a)~(f) are electric intensity distribution  $|E_x|^2$  for  $E_\perp$  wave in z-y, x-z, and x-y plane, respectively. The numerical computational analysis of the electromagnetic field is carried out using finite-difference and time-domain (FDTD) algorithm. It can be seen that focused spot size [full width at half maximum (FWHM)] at y-z plane is smaller than the one at x-y plane. For conventional Fresnel zone plate, when zone numbers are few, the first sidelobe is large. In contrast, our PMZP has much lower first sidelobe. Suppressed sidelobe at y-z plane is higher than the one at XOZ plane due to the incident wave with  $E_\perp$  wave. Transmission with the  $E_\perp$  wave illumination is extraordinarily enhanced due to the excited SPP wave coupling which is then converted to propagation wave by diffraction. Figure 2 (f) shows that there is only one peak transmission after exit plane of the Ag film. Furthermore, Fabry-Pérot-like phenomenon is found through the central aperture during the SPP wave coupling and propagation in cavity mode, as shown in Figs.17 (a), (b) and (f). It plays a positive role for the enhancement transmission.

Further characterization of the plasmonic lens was done, as shown in Figs. 19 (a)-(d) [42]. The Au thin film of 200 nm in thickness was coated on quartz substrate using e-beam evaporation technique. The lens was fabricated using focused ion beam (FEI Quanta 200 3D dual beam system) direct milling technique, as shown in Fig. 19 (b). Geometrical characterization was performed using an atomic force microscope (Nanoscope 2000 from DI company). Figure 19 (c) shows topography of the FIB fabricated plasmonic lens. The optical measurement was performed with a near-field optical microscope (MultiView 2000<sup>TS</sup> from Nanonics Inc. in Israel) where a tapered single mode fiber probe, with an aperture diameter of 100 nm, was used working in collection mode. The fiber tip was raster scanned at a discrete constant height of 500 nm, 1.0  $\mu\text{m}$ , 1.5  $\mu\text{m}$ , 2.0  $\mu\text{m}$ , 2.5  $\mu\text{m}$ , 3.0  $\mu\text{m}$ , 3.2  $\mu\text{m}$ , 3.5  $\mu\text{m}$ , 3.7  $\mu\text{m}$ , 4  $\mu\text{m}$ , 4.5  $\mu\text{m}$ , and 5  $\mu\text{m}$ , respectively, above the sample surface, and allowing us to map the optical intensity distribution over a grid of 256×256 points spanning an area of 20×20  $\mu\text{m}^2$ . Working wavelength of the light source is 532 nm (Nd: YAG laser with power of 20 mW). Additionally, a typical lock-in amplifier and optical chopper were utilized to maximize the signal-to-noise ratio. Figure 19 (d) shows the measured three-dimensional (3D) electric field intensity distribution of the lens at propagation distance of 2.5  $\mu\text{m}$ .

Figure 20 is a re-plotted 3D image of the NSOM measured intensity profiles along x-axis probed at the different propagation distance z ranging from 5 nm to 5  $\mu\text{m}$ . It intuitively shows the intensity distribution along propagation distance. It can be seen that the peak intensity is significantly enhanced from 0.01  $\mu\text{m}$  to 1  $\mu\text{m}$ , and then degraded gradually in near-field region because of SPP-enhanced wave propagation on Au surface vanished in free space when  $z > 1 \mu\text{m}$ . Only the interference-formed beam focusing region exists in near-field region. It is also in agreement with our calculated results. For more information, please see Ref. [43].

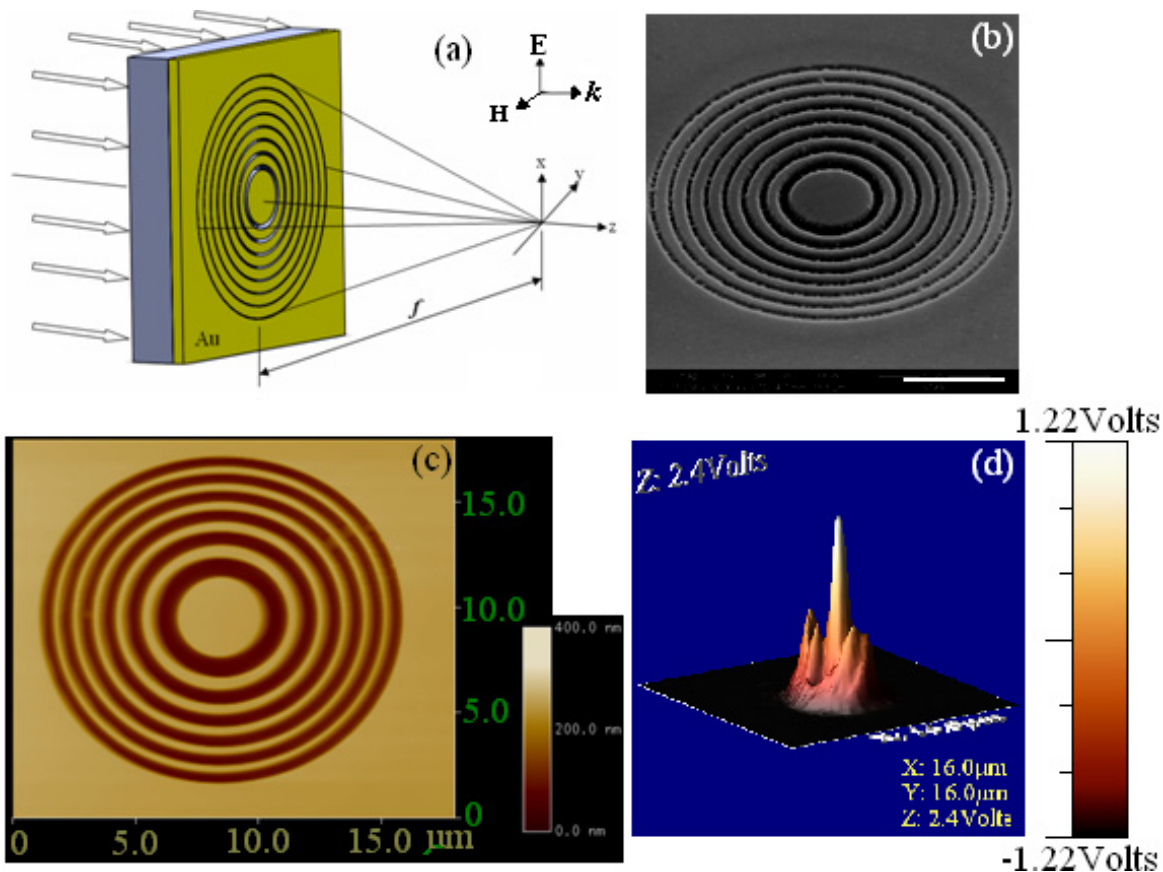


**Figure 19.** (a) Schematic diagram of the sandwiched plasmonic lens with chirped circular slits corrugated on Au film. Width of the outmost circular slit is 95 nm. Lens dimension (outer diameter) is 12  $\mu\text{m}$ . (b) Scanning electron microscope image of the lens fabricated using focused ion beam milling technique. The scale bar is 4  $\mu\text{m}$ . (c) AFM measurement result: topography of the fabricated lens. (d) NSOM characterization result of the lens: 2D E-field intensity distribution at propagation distance of 2.5  $\mu\text{m}$

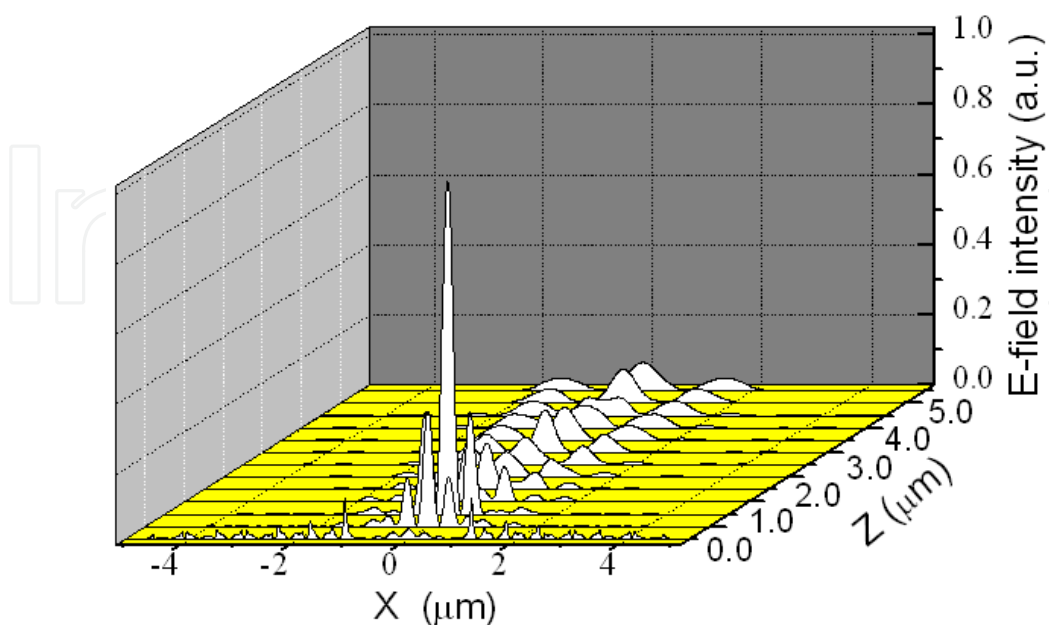


**Figure 20.** Measured 3D E-field intensity distribution of the plasmonic lens vs. lateral  $x$  and propagation distance  $z$  using NSOM. The figure was replotted using the NSOM probed data.

A hybrid Au-Ag subwavelength metallic zone plate-like structure was put forth for the purpose of preventing oxidation and sulfuration of Ag film, as well as realizing superfocusing, as shown in Fig. 21 [43]. The Au film acts as both a protector and modulator in the structure. Focusing performance is analyzed by means of three-dimensional (3D) finite-difference and time-domain (FDTD) algorithm-based computational numerical calculation. It can be tuned by varying thicknesses of both Au and Ag thin films. The calculated results show that thickness difference between the Au and Ag thin films plays an important role for transmission spectra. The ratio of Au to Ag film thicknesses,  $h_{Au}/h_{Ag}$ , is proportional to the relevant peak transmission intensity. In case of  $h_{Au} \approx h_{Ag} = 50$  nm, both transmission intensity and focusing performance are improved. In addition, the ratio  $h_{Au}/h_{Ag}$  strongly influences position of peak wavelengths  $\lambda_{Au}$  and  $\lambda_{Ag}$  generated from beaming through the metallic structures.

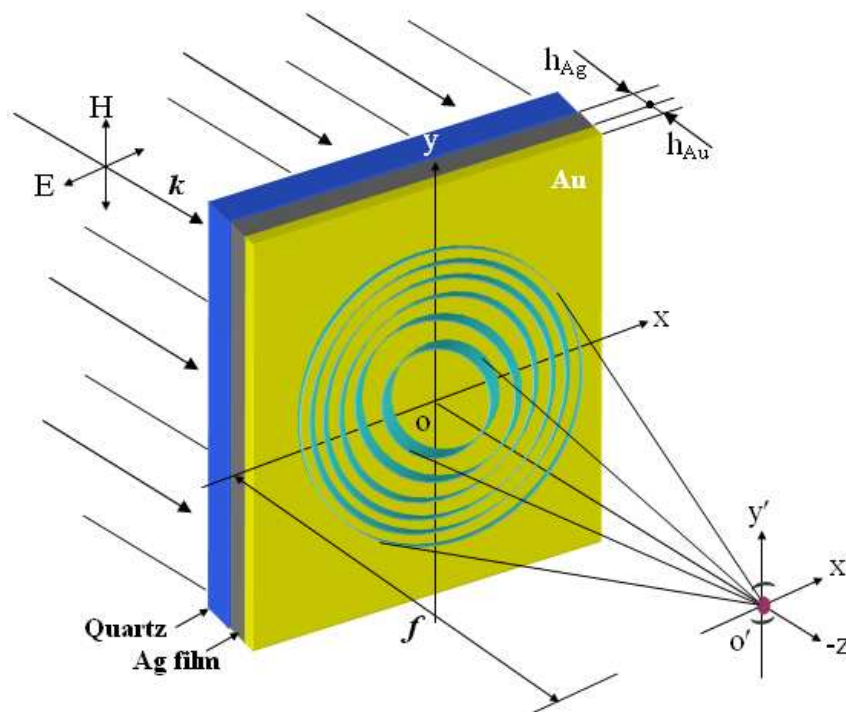


**Figure 21.** Schematic of the plasmonic micro-zone plate super-focusing with focal length  $f$ . It is illuminated by a plane wave with 633 nm incident wavelength. In our FDTD simulations the perfectly matched layer (PML) boundary condition was applied at the grid boundaries.

The following features were found from the calculation results:

1. Thickness difference between the Au and Ag thin films plays important role for transmission spectra. It determines peak transmission intensity. Ratio of film thicknesses  $\alpha = h_{Au}/h_{Ag}$  is proportional to the relevant peak intensity. It may attributed to the resonant wavelength of the hybrid structure which is proportional to  $\alpha$ .
2. In the case of  $h_{Au} \approx h_{Ag} = 50$  nm,  $\alpha \approx 1$ , both transmission intensity and focusing performance are improved in comparison to the other cases (fixing  $h_{Au} = 50$  nm and varying  $h_{Ag}$  from 10 nm to 200 nm).
3. For  $h_{Ag} = 200$  nm, both transmission intensity and focusing performance are improved gradually with increasing  $h_{Au}$ . However, unlike the fixed 200 nm thickness of the Ag

film, fixing  $h_{\text{Au}} = 50$  nm and 200 nm respectively and varying  $h_{\text{Ag}}$ , the corresponding optical performances are not improved gradually with increasing  $h_{\text{Ag}}$ .

4. Ratio  $\alpha = h_{\text{Au}}/h_{\text{Ag}}$  strongly influences position of peak wavelengths  $\lambda_{\text{Au}}$  and  $\lambda_{\text{Ag}}$  generated from the metallic subwavelength structures.

The calculation results show that thickness of both the Au and Ag thin films has significant tailoring function due to the great contribution to superfocusing and transmission. Improved focusing performance and enhanced transmission can be obtained if  $h_{\text{Au}}$  and  $h_{\text{Ag}}$  match each other. This hybrid subwavelength structure has potential applications in data storage, nanophotolithography, nanometrology, and bio-imaging etc.

However, the rings-based structures have higher sidelobes. To suppress the sidelobes, a circular holes-based plasmonic lens was reported, as shown in Fig. 22 [44]. In the plasmonic lens with fixed pinhole diameters, propagation waves still exist for much reduced periodicity of pinholes due to the SPPs wave coupling, which interferes with the diffraction wavelets from the pinholes to form a focusing region in free space. Increasing incident wavelength is equivalent to reducing the pinhole diameters, and rapid decay of the EM field intensity will occur accordingly. The superlens proposed by the authors has the advantages of possessing micron scale focal length and large depth of focus along the propagation direction. It should be especially noted that the structure of the superlens can be easily fabricated using the current nanofabrication techniques, e.g. focused ion beam milling and e-beam lithography.

To further improve focusing quality of the circular holes-based plasmonic lens, an elliptical nanoholes-based plasmonic lens was put forth, as shown in Fig. 9 [45]. The plasmonic lens is

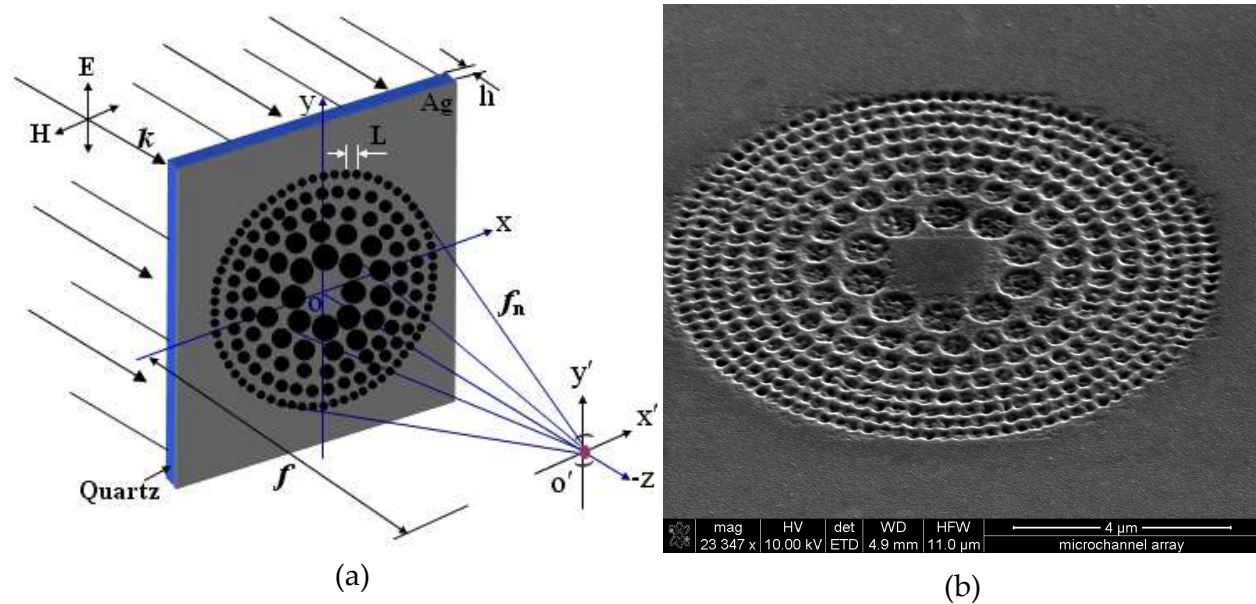


**Figure 22.** (a) Schematic of the pinhole array with focal length  $f$ . Lateral central distance  $L$  determines wave coupling between the neighboring holes. The pinholes are uniformly distributed in the zones. It is illuminated by a plane wave with 633 nm incident wavelength and p-polarization (transverse-magnetic field with components of  $E_x$ ,  $H_y$ , and  $E_z$ ). The perfectly matched layer (PML) boundary condition was applied at the grid boundaries in the three-dimensional FDTD simulation. (b) Nanofabrication of the lens using focused ion beam.



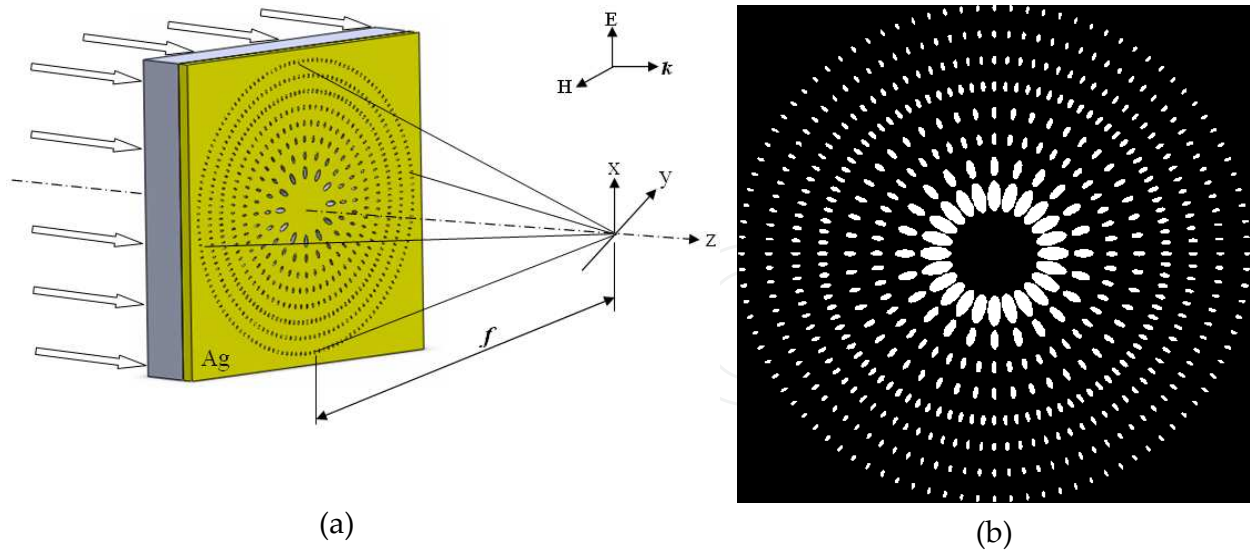


**Figure 23.** (a) Schematization of the pinhole array with focal length  $f$ . Lateral central distance  $L$  determines of wave coupling between the neighbored holes. The pinholes are uniformly distributed along the zones. It is illuminated by various waves with 633 nm incident wavelength. And we have different polarization states such as TM, EP and RP. (b) layout of elliptical pinholes with total 8 rings  $\delta = 0.6$  being used in our computational numerical calculation.

composed of elliptical pinholes with different sizes distributed in different rings with variant periods. Long-axis of the ellipse is defined as  $a_n=3w_n$ , whereas  $w_n$  is width of the corresponding ring width, and  $n$  is the number of rings. A thin film of Ag coated on the glass substrate is perforated by the pinholes. The numbers of  $w_n$  and radius for different rings are listed in Table1.

Ring No.	1	3	3	4	5	6	7	8
Ring radius( $\mu\text{m}$ )	1.41	2.11	2.78	3.43	4.08	4.73	5.37	6.01
$w_n$ (nm)	245	155	116	93	78	67	59	53

**Table 1.** The numbers of  $w_n$  for different rings with orders from inner to outer (designed  $f=1\mu\text{m}$ )

As an example, the authors studied the case of 200 nm thickness Ag film coated on quartz substrate and designed a nanostructure with 8 rings on the metal film (see Fig. 23). The pinholes are completely penetrated through the Ag film. The number of pinholes from inner to outer rings is 8, 20, 36, 55, 70, 96, 107, and 140, respectively. Outer diameter of the ring is 12.05  $\mu\text{m}$ . Radius of the rings can be calculated by the formula  $r_n^2 = 2nf\lambda + n^2\lambda^2$ , where  $f$  is the focal length for working wavelength of  $\lambda=633$  nm which we used in our works. For simplicity, we define a ratio of short-axis to long-axis  $\delta= b/a$  (where  $a$  is the length of long-axis of the elliptical pinholes, and  $b$  the short-axis). The used metal here is Ag with dielectric constant of  $\epsilon_m = -17.24 + i0.498$  at  $\lambda=633$  nm, and  $\epsilon_d=1.243$  for glass. The incident angle  $\theta$  is  $0^\circ$  (normal incidence). In our analysis, we simulated the cases of the ratios:  $\delta = 0.1, 0.2$ , and  $0.4$ , respectively. The ultra-enhanced lasing effect disappears when the ratio  $\delta \rightarrow 1$  (circular pinholes). Orientation of the pinholes is along radial direction. The pinholes symmetrically

distribute in different rings with variant periods. It can generate ultra-enhanced lasing effect and realize a long focal length in free space accordingly with extraordinarily elongated depth of focus (*DOF*) of as long as 13  $\mu\text{m}$  under illumination of plane wave in linear y-polarization.

Figure 24 shows our computational results: E-field intensity distribution  $|E_y|^2$  at x-z and y-z planes for (a) and (b)  $\delta=0.1$ ; (c) and (d)  $\delta=0.2$ ; and (e) and (f)  $\delta=0.4$ , respectively. It can be seen that E-field intensity distribution is symmetric due to linear y-polarization which is formed by uniformly rotating linear polarization radiating along radial directions. By means of interfering constructively, and the  $E_z$  component interferes destructively and vanishes at the focus. Thus we have  $|E|^2=|E_x|^2+|E_y|^2+|E_z|^2=|E_y|^2$ , whereas  $E_x=0$ , and  $E_z=0$ . The lasing effect-induced ultra-long *DOF* is 7  $\mu\text{m}$ , 12  $\mu\text{m}$ , and 13  $\mu\text{m}$  for  $\delta=0.1$ , 0.2, and 0.4, respectively. It is three orders of magnitude in comparison to that of the conventional microlenses. The ultra-enhanced lasing effect may attribute to the surface plasmon (SP) wave coupling in the micro- and nano-cavity which form Fabry-Pérot resonance while the beam passing through the constructive pinholes. Calculated full-width and half-maximum (FWHM) at propagation distance  $z=-7\text{ }\mu\text{m}$  in free space is 330 nm, 510 nm, and 526 nm for  $\delta=0.1$ , 0.2, and 0.4, respectively.

Lasing effect of the plasmonic lens with extraordinarily elongated *DOF* has the following unique features in practical applications:

1. In bioimaging systems such as confocal optical microscope, three-dimensional (3D) image of cells or molecular is possible to be obtained and conventional multilayer focal plane scanning is unnecessary.
2. In online optical metrology systems, feed-back control system can be omitted because height of surface topography of the measured samples as large as ten micron is still within the extraordinarily elongated *DOF* of the plasmonic lenses.
3. In plasmonic structures-based photolithography systems, the reported experimental results were obtained at near-field with tens nanometers gap between the structure and substrate surface. Apparently, it is difficult to control the gap in practical operation. However, using this plasmonic lens, the working distance between the structure and substrate surface can be as long as 12  $\mu\text{m}$  and even longer. Practical control and operation process will be much easier and simplified than the approaches before in case of using this lens.

Like the discussion above regarding illumination with different polarization states, influence of polarization states on focusing properties of the the plasmonic lenses with both chirped circular slits and elliptical nanopinhole were reported [46, 47].

The lens was fabricated using focused ion beam directly milling technique, and characterization of the elliptical nanopinhole-based plasmonic lens was carried out using NSOM, as shown in Figs. 25 (a) and (b). Currently, this work is still in progress in the research group.

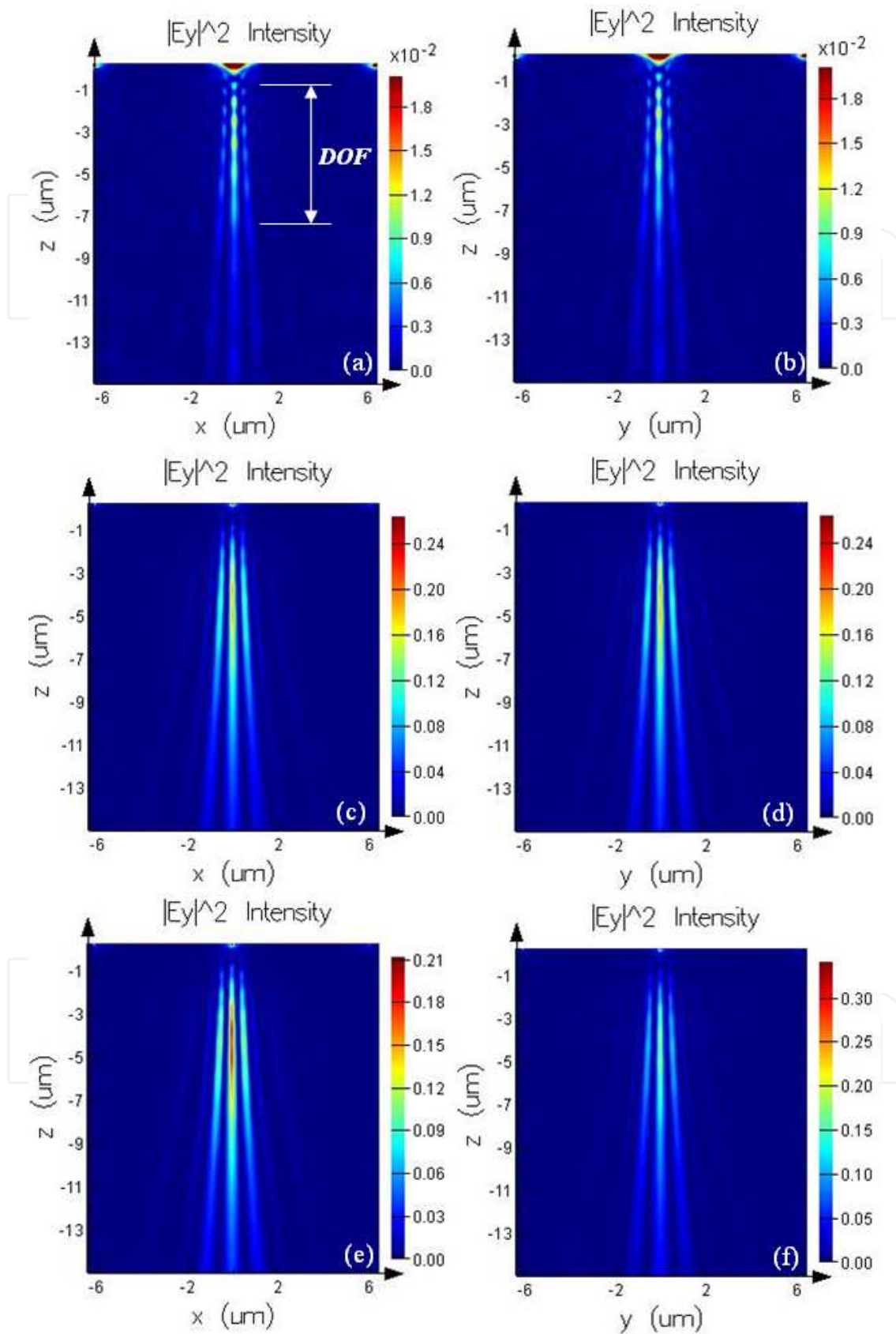


**Figure 24.** E-field intensity distribution  $|E_y|^2$  at x-z and y-z planes for (a) and (b)  $\delta=0.1$ ; (c) and (d)  $\delta=0.2$ ; and (e) and (f)  $\delta=0.4$ , respectively.

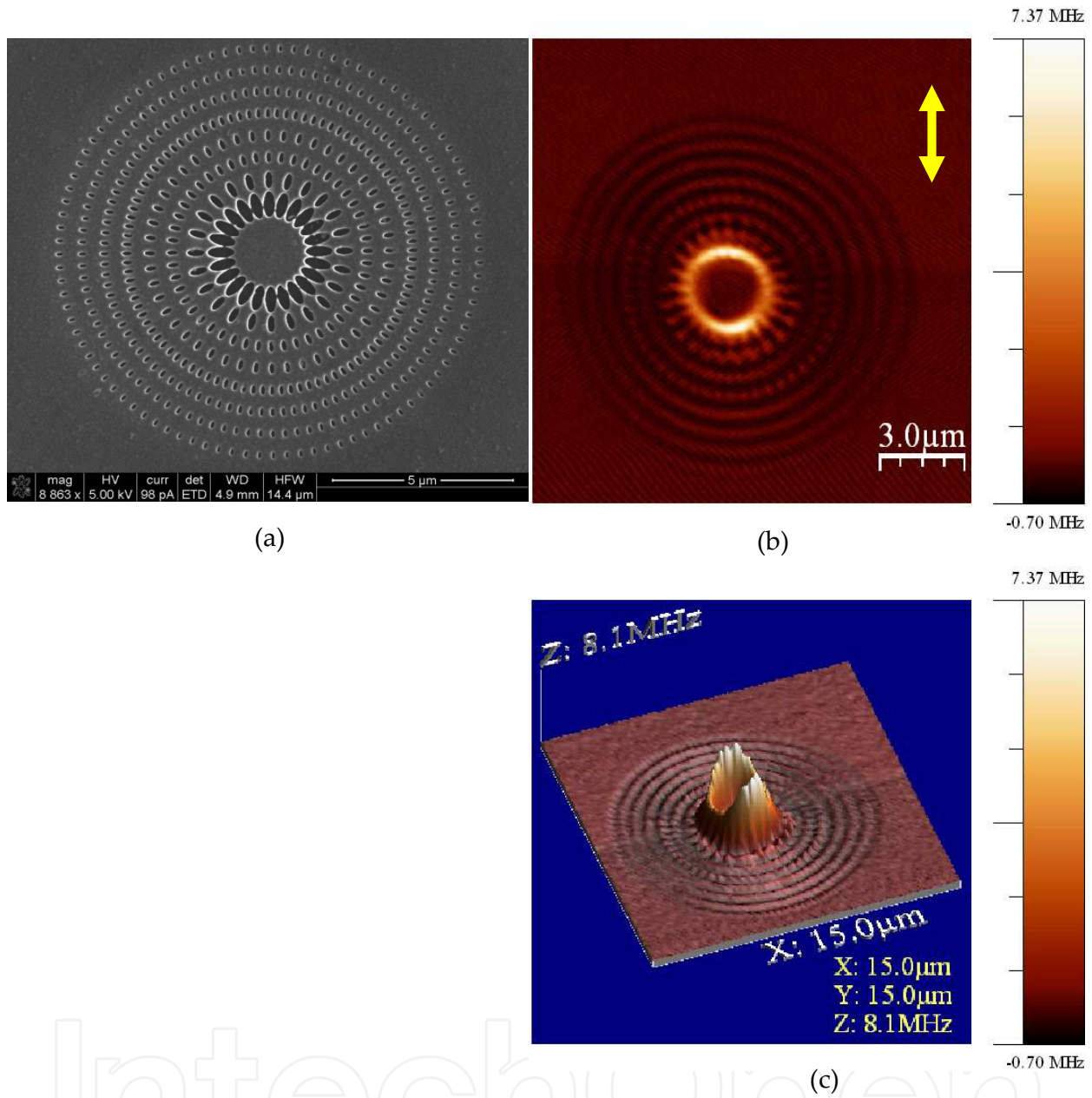


**Figure 25.** (a) SEM micrograph of the elliptical nanopinhole-based plasmonic lens. (b) 2D image of NSOM probing along propagation distance at  $z=20\text{nm}$  in free space. The arrow indicates direction of linear polarization. (c) 3D image of NSOM probing.

Here we addressed an issue here from fabrication point of view. Real part of Au permittivity  $\epsilon_{\text{Au}}$  will be increased due to  $\text{Ga}^+$  implantation of the FIB directly etching process. Theoretically, propagation constant  $k_{\text{SP}}$  will be increased due to the large real part of dielectric constant as  $k_{\text{SP}} = \frac{\omega}{c} \sqrt{\frac{\epsilon_m \epsilon_d}{\epsilon_m + \epsilon_d}}$ , whereas  $\omega$  is the incident frequency,  $c$  is the speed of light in vacuum,  $\epsilon_m$  and  $\epsilon_d$  is dielectric constant of metal and dielectric, respectively. The increased  $k_{\text{SP}}$  will cause strong transmission enhancement and generate extended skin depth



in free space which is helpful for formation of the focusing region and makes a positive contribution on the plasmonic focusing accordingly.

An elliptical nano-pinholes-based plasmonic lens was studied experimentally by means of FIB nanofabrication, AFM imaging, and NSOM characterization for the purpose of proof of plasmonic finely focusing. Both modes of sample scan and tip scan were employed for the lens probing. For the NSOM-based optical characterization of the plasmonic lenses, both of them have their own characteristics. The former can generate a bright-field like image with strong and uniform illumination; and the latter can produce a dark-field like image with high contrast which is helpful for checking focusing performance of the lenses. Our experimental results demonstrated that the lens is capable of realizing a subwavelength focusing with elongated depth of focus.

### 3.1.2.3. Illumination under radial polarization state

Most recently, the circular rings-based plasmonic lens was experimentally demonstrated [48, 49]. The focusing of surface plasmon polaritons by a plasmonic lens illuminated with radially polarized light was investigated. The field distribution is characterized by near-field scanning optical microscope. A sharp focal spot corresponding to a zero-order Bessel function is observed. For comparison, the plasmonic lens is also measured with linearly polarized light illumination, resulting in two separated lobes. Finally, the authors verify that the focal spot maintain sits width along the optical axis of the plasmonic lens. The results demonstrate the advantage of using radially polarized light for nanofocusing applications involving surface plasmon polaritons. Figures 26 (a) and (b) are reported NSOM characterization results. For comparison purposes, this theoretical cross section is also shown in Figure 26 (b). The profile of the Bessel function can be clearly observed. Neglecting the contribution of the E component, the theoretical spot size (based on full width half-maximum criterion) is 380nm. The measured spot size is slightly larger,  $410 \pm 39\text{nm}$  (error was estimated by taking several cross sections through the center of the PL along different directions).

## 3.2. Subwavelength metallic structure for imaging

A planar lens based on nanoscale slit arrays in a metallic film is present here for subwavelength imaging in the far field. Figure 27 is the schematic of the optical imaging with metallic slab lens [51]. To illustrate the design, both object distance  $a$  and image distance  $b$  are set to be  $1\text{ }\mu\text{m}$ . The aperture and the thickness of silver slab lens are  $3\text{ }\mu\text{m}$  and  $300\text{ nm}$  respectively. The permittivity  $\epsilon_m = -29.26 + i1.348$  is used for silver at  $810\text{ nm}$ .

When the light with magnetic field polarized in the  $y$  direction impinged on the surface of silver slab, SPPs can be excited at the slit entrance. The SPPs propagate inside the slits in the specific waveguide modes until reaching the export where we radiate into free space and form the optical image at the desired position. For the imaging of object localized on the axis  $x=0$ , the phase retardation of light transmitted through the lens is given by

$$\Delta\phi(x) = 2n\pi + \Delta\phi(0) + \frac{2\pi}{\lambda}(a+b - \sqrt{a^2+x^2} - \sqrt{b^2+x^2}) \quad (4)$$

where  $n$  is an integer number. Therefore, the key point of designing the metallic lens is to determine the width and position of slits for appropriate phase retardation.

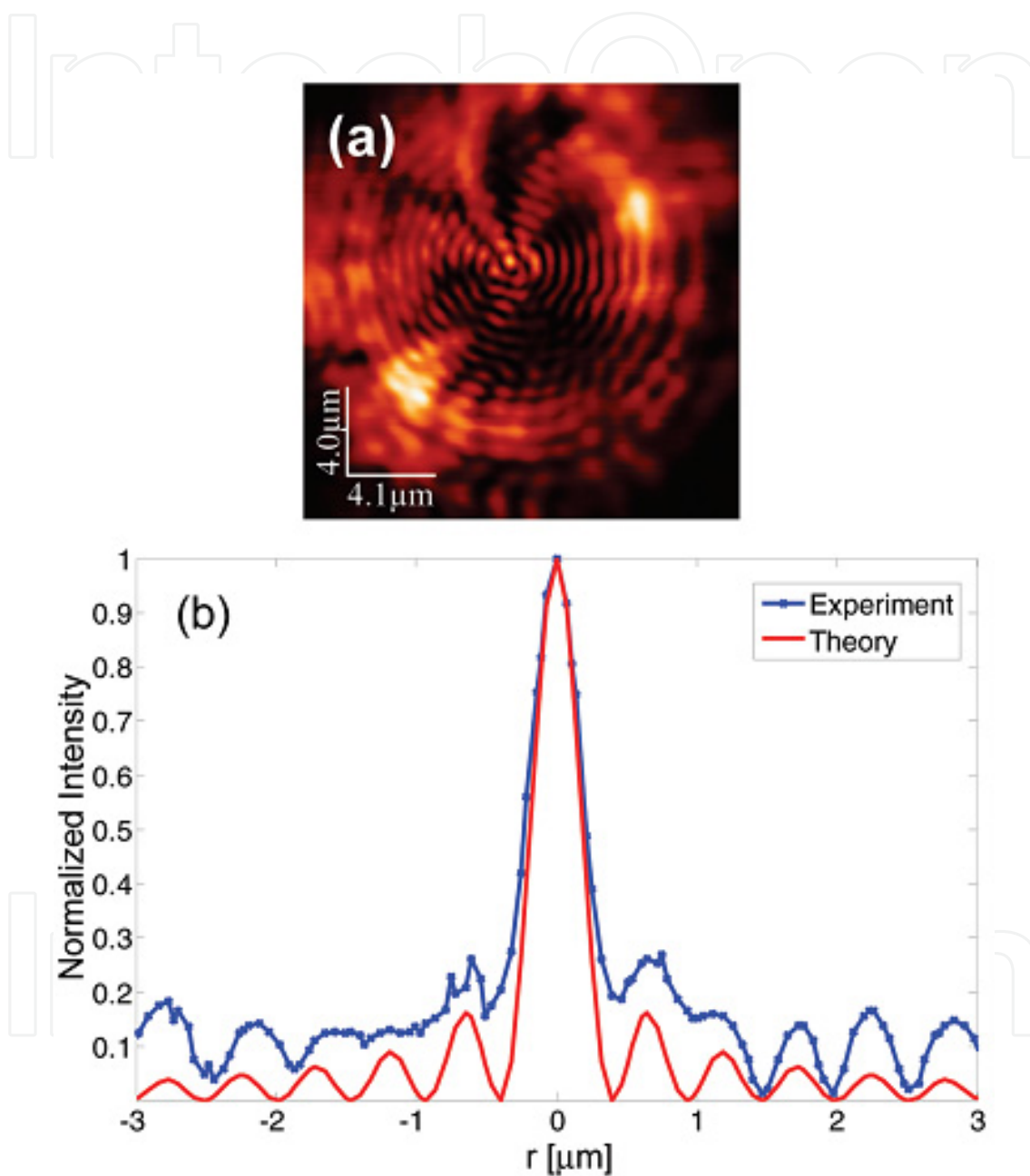


**Figure 26.** NSOM measurement showing SPP focusing in the plasmonic lens illuminated by radially polarized light. The NSOM probe was at a constant height of 2  $\mu\text{m}$  above the PL. (a) 2D NSOM scan. Bright regions correspond to high intensity. (b) Normalized experimental (blue, cross markers) and theoretical (red, solid line) cross sections through the center of the PL. The sharp focus can be clearly observed. Reprinted with permission from “Gilad M.Lerman, Avner Yanai, and Uriel Levy, *Nano Lett.* 9, 2139-2143 (2009).” of copyright ©2009 Chemical Society of American.

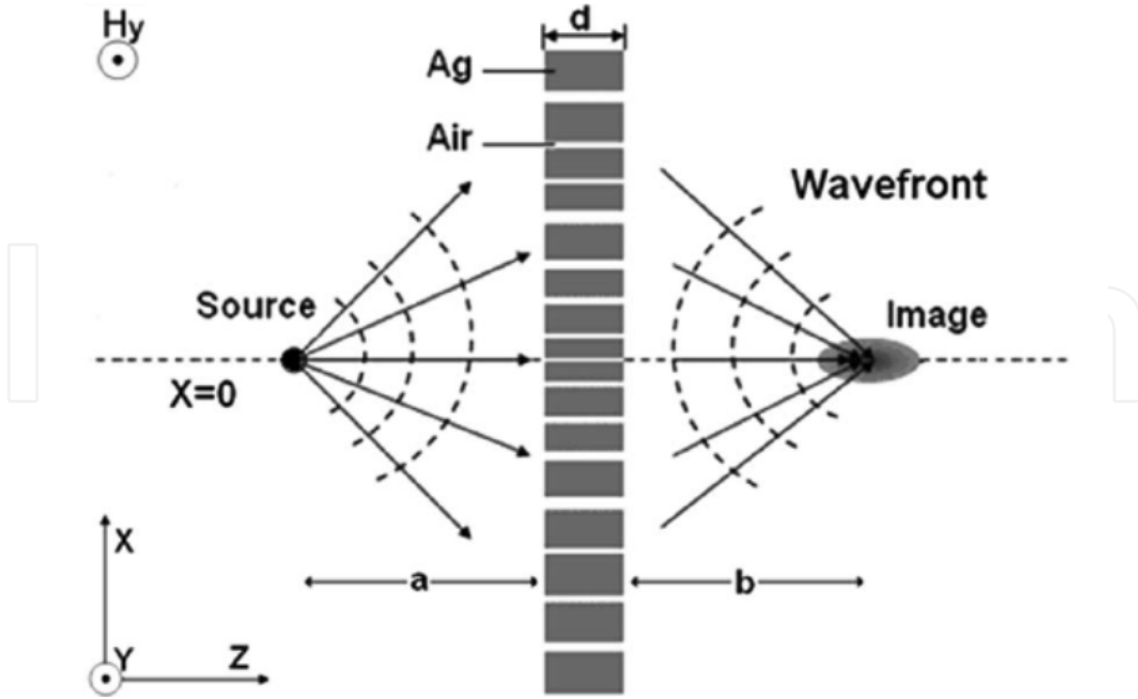


**Figure 27.** A schematic of optical imaging by a metallic slab lens with nanoslits. Reprinted with permission from “Ting Xu, et. al. Appl. Phys. Lett. 91,201501 (2007)” of copyright ©2007 American Institute of Physics.

Because of the complexity of the accurate description of the processes of SPPs’ excitation, propagation, and coupling in metallic slits, the convenient and effective way is the approximation of these processes and making sure of good accuracy simultaneously. The coupling of SPPs during the propagation in slits is neglected, provided that the metallic wall between any two adjacent slits is larger than the skin depth in metal, about 24 nm for silver at a wavelength of 810 nm given by

$$Z = \frac{1}{k_0} \left[ \frac{\text{Re}(\epsilon_m) + \epsilon_d}{\text{Re}(\epsilon_m)^2} \right]^{1/2} \quad (5)$$

The coupling effect occurred at the exit surface from neighboring slits is also omitted, compared with the intensity of directly radiated light from slits. The design above also displays that only a slight deviation is produced by coupling effect and it affects the image profile insignificantly. Assuming that the slit width is much smaller than a wavelength, it is justified to only consider the fundamental mode in the slit. Its complex propagation constant  $\beta$  in the slit is determined by the following equation:

$$\tanh(\sqrt{\beta^2 - k_0^2 \epsilon_d} w / 2) = \frac{-\epsilon_d \sqrt{\beta^2 - k_0^2 \epsilon_m}}{\epsilon_m \sqrt{\beta^2 - k_0^2 \epsilon_d}} \quad (6)$$

where  $k_0$  is the wave vector of light in free space,  $\epsilon_m$  and  $\epsilon_d$  are the permittivity of the metal and dielectric material inside the slits, and  $w$  is the slit width. The real and imaginary parts

of  $\beta$  determine the phase velocity and the propagation loss of SPPs inside the metallic slit, respectively.

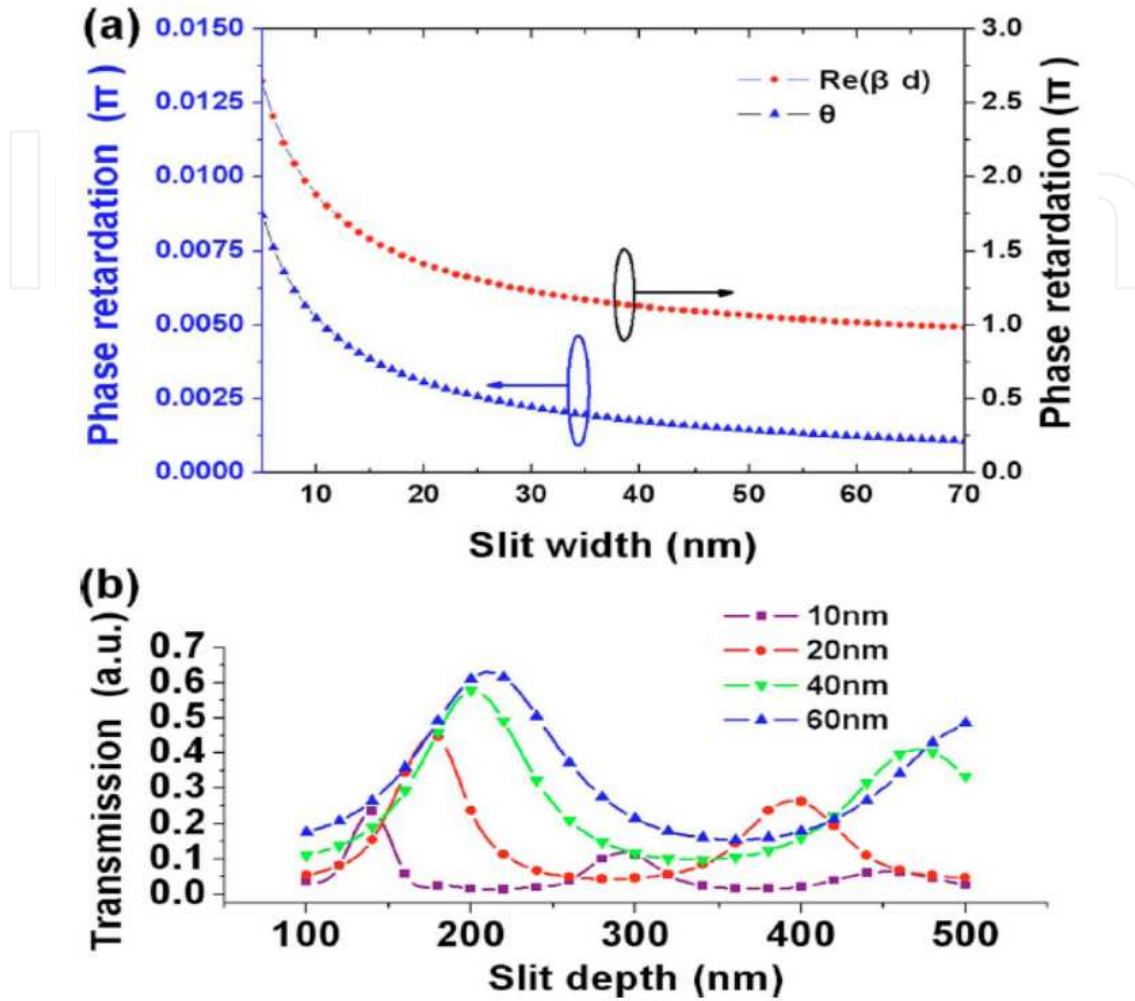


**Figure 28.** (a) Dependence of phase retardation on the slit width. Red and blue tags represent the contributions for phase retardation from the real part of propagation constant and multiple reflections. The wavelength of incident light is 810 nm. (b) Transmittance of optical field (810 nm wavelength) through a nanoslit vs the slit depth ranging from 100 to 500 nm. Slit widths are 10, 20, 40, and 60 nm. Reprinted with permission from “Ting Xu, et. al. Appl. Phys. Lett. 91,201501 (2007)” of copyright ©2007 American Institute of Physics.

To illustrate the validity of metallic slab lens, finite-difference time-domain simulations are performed. Figure 28 (a) illuminates the dependence of phase retardation on slit width. Figure 28 (b) plots the finite-difference time-domain (FDTD) simulated transmittance of light through a slit with variant thickness as ranging from 100 to 500 nm by normal incidence at the wavelength of 810 nm. Calculated steady optical field (the magnetic field  $|\text{Hy}|^2$ ) of the simulation result is shown in Fig. 29. Obvious image spot can be seen at the position around  $Z=2.43 \mu\text{m}$  with the full width at half maximum of 396 nm approximately half of the incident wavelength. The slight focal shift of about 60 nm. Above all, the metallic slab lens displays a considerably good performance for imaging objects in the far field region.



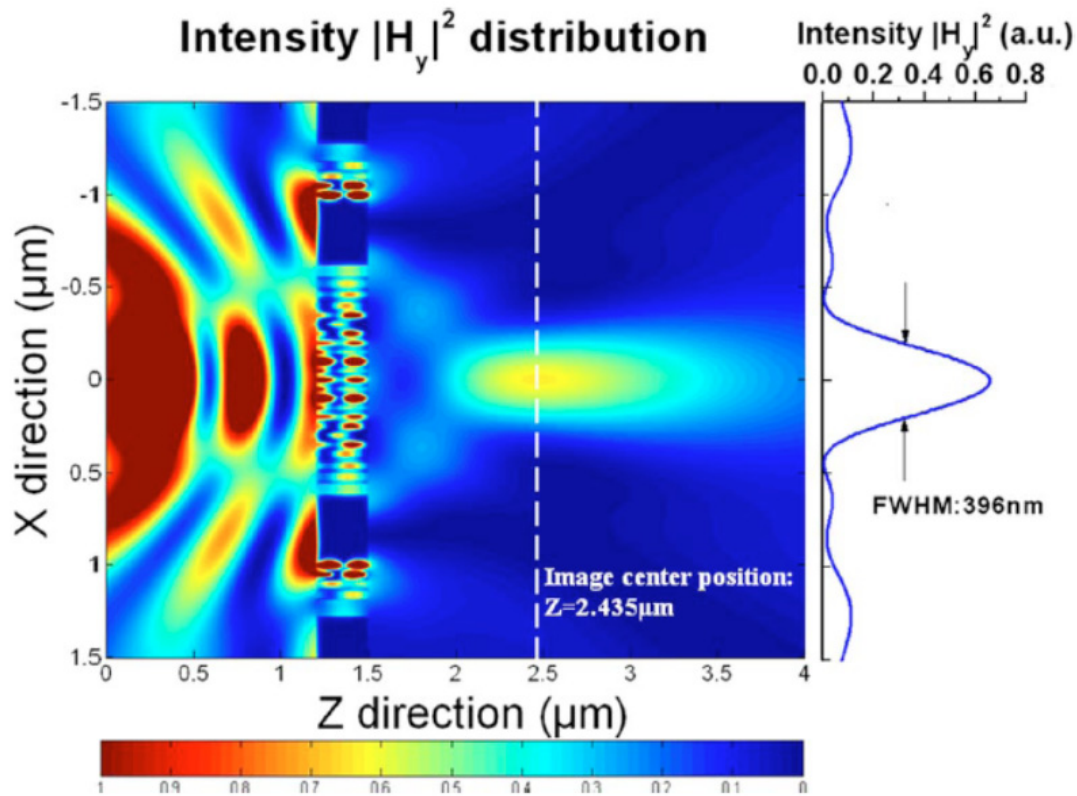


**Figure 29.** Calculated steady magnetic field intensity  $|H_y|^2$  of the simulation results using FDTD method. The sprirce is localized at  $X=0$  and  $Z=0.2 \mu\text{m}$ . The metallic slab lens ranged from  $Z=1.2 \mu\text{m}$  to  $Z=1.5 \mu\text{m}$ . The radiated light from the source is TM polarized with a wavelength of  $810\text{nm}$ . The curve at the right side represents the cross section of image plane at  $Z=2.435 \mu\text{m}$ . Reprinted with permission from "Ting Xu, et. al. Appl. Phys. Lett. 91,201501 (2007)" of copyright ©2007 American Institute of Physics.

In addition, nanorod array was reported being used for imaging [51]. Mark et. al reported parallel conducting wires as a lens for subwavelength microwave imaging [52].

#### 4. Plasmonic Lens on the basis of waveguide modes

Another structure that can realize nanofocusing was theoretically reported [53]. SPPs propagating toward the tip of a tapered plasmonic waveguide are slowed down and asymptotically stopped when we tend to the tip, never actually reaching it (the travel time to the tip is logarithmically divergent). This phenomenon causes accumulation of energy and giant local fields at the tip. Focusing of fundamental cylindrical SPP wave is formed at apex of the taper tip, as shown in Fig. 30. Figure 31 displays the amplitudes of the local optical fields in the cross section of the system for the normal and longitudinal (with respect to the axis) components of the optical electric field. As SPP's move toward the tip, the SPP fields start to localize at the metal surface, and simultaneously, our wavelength is progressively reducing and amplitude growing. The field magnitudes grow significantly at small  $|Z|$ . The transverse  $x$  component grows by an order of magnitude as the SPP's approach the tip of the guide, while the longitudinal  $z$  component, which is very small far

from the tip, grows relatively much stronger. The 3D energy concentration occurs at the tip of a smoothly tapered metal nanoplasmonic waveguide. This causes the local field increase by 3 orders of magnitude in intensity and four orders in energy density.

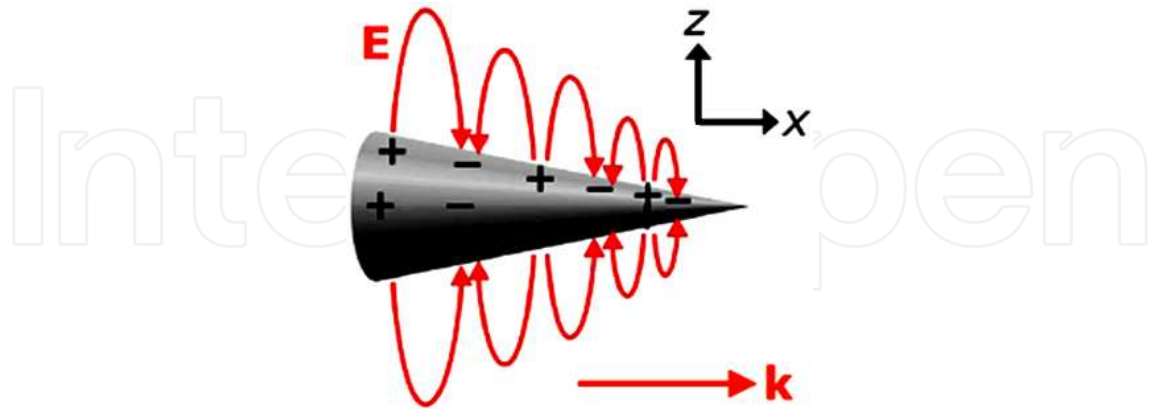


**Figure 30.** Geometry of the nanoplasmonic waveguide. The radius of the waveguide gradually decreases from 50 nm to 2 nm. Reprinted with permission from “Mark I. Stockman, Phys. Rev. Lett. 93, 137404 (2004)” with copyright © 2004 of American Society of Physics.

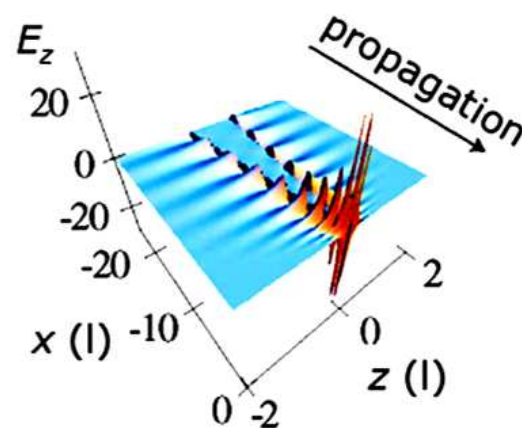


**Figure 31.** Snapshot of instantaneous fields (at some arbitrary moment  $t=0$ ): longitudinal component  $E_z$  of the local optical electric field are shown in the longitudinal cross section ( $xz$ ) plane of the system. The fields are in the units of the far-zone (excitation) field. Reprinted with permission from “Mark I. Stockman, Phys. Rev. Lett. 93, 137404 (2004)” with copyright © 2004 of American Society of Physics.

Most recently, Ewold *et. al.* reported our tapered waveguide structure for nanofocusing, as shown in Fig. 32 [54]. It was used for focusing of surface plasmon polaritons (SPPs) excited with 1.5  $\mu\text{m}$  light in a tapered Au waveguide on a planar dielectric substrate by experiments and simulations. We find that nanofocusing can be obtained when the asymmetric bound mode at the substrate side of the metal film is excited. The propagation and concentration of this mode to the tip is demonstrated. No sign of a cutoff waveguide width is observed as the SPPs propagate along the tapered waveguide. Simulations show that such concentrating behavior is not possible for excitation of the mode at the low-index side of the film. The mode that enables the focusing exhibits a strong resemblance to the asymmetric mode responsible for focusing in conical waveguides. This work demonstrates a practical implementation of plasmonic nanofocusing on a planar substrate.

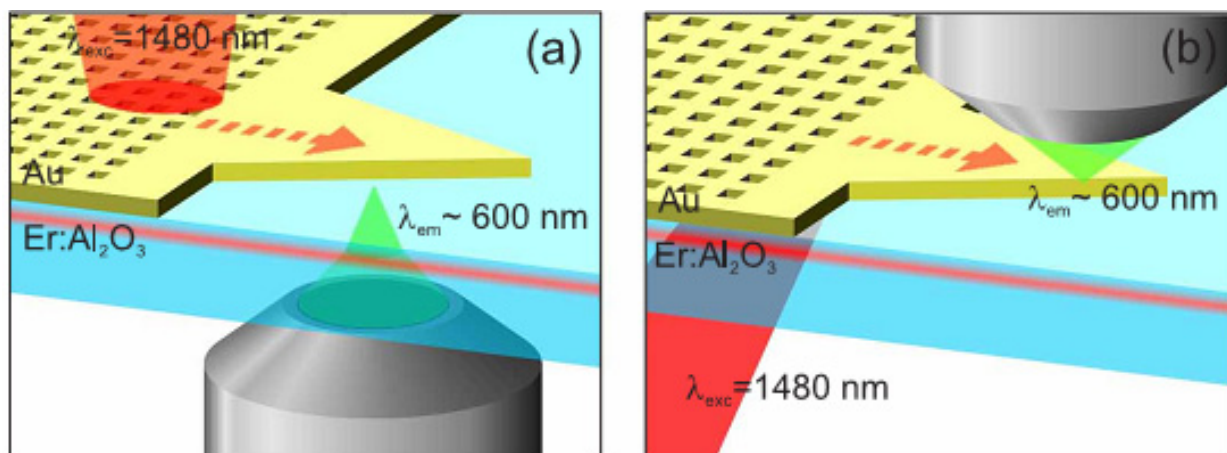


**Figure 32.** Schematic of the experimental geometry in the case of upconversion luminescence detection through the substrate (a), or from the air side of the sample (b). In both cases the SPPs are excited with infrared light at the Au/Al<sub>2</sub>O<sub>3</sub> interface in the direction of the arrow. The red line schematically indicates the Er depth profile. Reprinted with permission from “Ewold Verhagen, Albert Polman, and L. (Kobus) Kuipers, *Opt. Express* 16, 45-57 (2008).” of copyright ©2008 Optical Society of American.

A fiber-pigtailed 1.48  $\mu\text{m}$  diode pump laser is used as excitation source. Figure 32 shows a schematic of the hole array/taper geometry. The pitch of the hole array is chosen such that p-polarized light with a wavelength of 1.48  $\mu\text{m}$  is diffracted to generate SPPs propagating at the substrate side of the film. To maximize the excitation of the desired SPP mode, the excitation beam is focused to a 10  $\mu\text{m}$  wide spot near the edge of the array. The triangular tapered waveguide starts at a distance of 6  $\mu\text{m}$  from the edge of the excitation array and has a base width of 12  $\mu\text{m}$  and a length of 60  $\mu\text{m}$  (taper angle 11°).

## 5. Plasmonic lens on the basis of curved chains of nanoparticles

Focusing of surface plasmon polaritons (SPPs) beams with parabolic chains of gold nanoparticles fabricated on thin gold films was reported [55]. SPP focusing with different parabolic chains is investigated in the wavelength range of 700-860 nm, both experimentally and theoretically. Mapping of SPP fields is accomplished by making use of leakage radiation microscopy, demonstrating robust and efficient SPP focusing into submicron spots. Numerical simulations based on the Green's tensor formalism show very good agreement with the experimental results, suggesting the usage of elliptical corrections for parabolic structures to improve our focusing of slightly divergent SPP beams.

Shortly after the above work, excitation, focusing and directing of surface plasmon polaritons (SPPs) with curved chains of nanoparticles located on a metal surface is investigated both experimentally and theoretically by Evlyukhin et. al., as shown in Fig. 33 [56]. We demonstrate that, by using a relatively narrow laser beam (at normal incidence) interacting only with a portion of a curved chain of nanoparticles, one can excite an SPPs beam whose divergence and propagation direction are dictated by the incident light spot size and its position along the chain. It is also found that the SPPs focusing regime is strongly influenced by the chain inter-particle distance. Extensive numerical simulations of



**Figure 33.** Scanning electron microscope (SEM) (a) the top image of the structure, (b) the image of the structure obtained with view angle  $45^\circ$ . The radius of curved chains of nanoparticles is equal to  $10\mu\text{m}$ . The particle in-plane size (diameter) and inter-particle distance are estimated to be about  $350\text{nm}$  and  $850\text{nm}$ , respectively, the particle height is  $300\text{nm}$ . Reprinted with permission from “A. B. Evlyukhin, et. al, Opt. Exp. 15, 16667-16680 (2007).” of copyright ©2007 Optical Society of American.

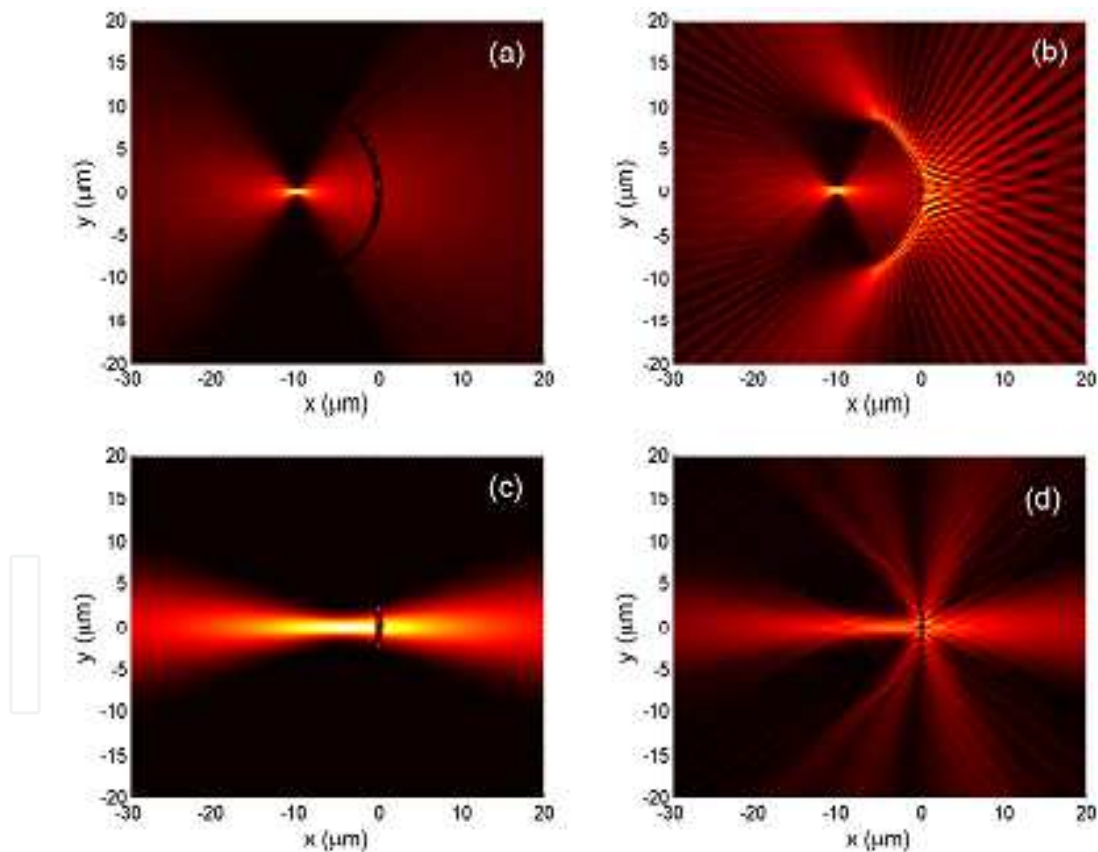


**Figure 34.** Magnitude of scattered electric field calculated above the gold surface with a curved chain (with  $R=10\mu\text{m}$  and  $\beta=60^\circ$ ) of spheroid gold nanoparticles illuminated by a light beam at the wavelength of  $800\text{nm}$  being incident perpendicular to the gold surface and polarized along  $x$ -direction. The waist  $W$  of the incident beam and the inter-particle (center-to-center) spacing  $D$  in the chain are (a)  $W=10\mu\text{m}$ ,  $D=400\text{nm}$ ; (b)  $W=10\mu\text{m}$ ,  $D=800\text{nm}$ ; (c)  $W=1.5\mu\text{m}$ ,  $D=400\text{nm}$ ; (d)  $W=1.5\mu\text{m}$ ,  $D=800\text{nm}$ . Reprinted with permission from “A. B. Evlyukhin, et. al, Opt. Exp. 15, 16667-16680 (2007).” of copyright ©2007 Optical Society of American.



the configuration investigated experimentally are carried out for a wide set of system parameters by making use of the Green's tensor formalism and dipole approximation. Comparison of numerical results with experimental data shows good agreement with respect to the observed features in SPP focusing and directing, providing the guidelines for appropriate choice of the system parameters.

When the inter-particle distance is smaller than the light wavelength, the pattern of the field magnitude distribution is relatively smooth [Fig. 34 (a)]. In this case, the illuminated part of the chain exhibits scattering properties that are similar to those of a continuous ridge. Note that straight ridges are frequently used for excitation of a divergent SPP beam on a metal surface in SPP experiments. When increasing the inter-particle distance, the individual particles of the chain become relatively independent sources of the scattered waves whose phases differ considerably, resulting in a complex interference pattern [Fig. 34 (b)] – a system of divergent SPPs rays. A similar trend is also seen for a relatively narrow incident light beam [see Figs. 34 (c) and (d)]. If the light spot size being determined by  $W$  is sufficiently small in comparison with the chain curvature radius  $R$  so that the diffraction angle of a SPPs beam is approximately equal to the focusing angle  $W/R$ , the focusing effect decreases and the maximum of SPPs intensity moves toward the nanoparticle chain. Strong SPPs focusing effects have been obtained for relatively larger  $W/R$ .

Apart from the chain particle-based plasmonic structures for nanofocusing, the reverse pattern: nanoholes, constructed in curved chains can also realize focusing of SPP wave, as shown in Fig. 35 [57]. The focused SPPs can be directly coupled into a waveguide located at the focal plane. The constructive interference of SPPs launched by nanometric holes allows us to focus SPP into a spot of high near-field intensity having subwavelength width. Near-field scanning optical microscopy is used to map the local SPP intensity. The resulting SPPs patterns and our polarization dependence are accurately described in model calculations based on a dipolar model for the SPP emission at each hole. Furthermore, we show that the high SPPs intensity in the focal spot can be launched and propagated on a Ag strip guide with a  $250 \times 50 \text{ nm}^2$  cross section, thus overcoming the diffraction limit of conventional optics. The combination of focusing arrays and nano-waveguides may serve as a basic element in planar nano-photonic circuits.

Not only focusing and imaging, the similar plasmonic structures can be used as beam splitters [58] and beam shaping [59]. Nanofabrication of the plasmonic lenses were reported in Ref. [60-62].

## 6. Plasmonic Talbot effect of nanolenses

Previous introduction in Section 3 shows a common phenomenon which there several focal points exist along central axis in free space after exit plane of the nanolenses.

To explore its physical mechanism, we compared the phenomenon to another well-known story: Talbot effect, *i.e.* self-imaging. The self-imaging means that when a one-dimensional (1D) periodic structure is illuminated by the monochromatic plane wave, the image of that structure can be observed at the periodical distance from the back side of the structure. It is

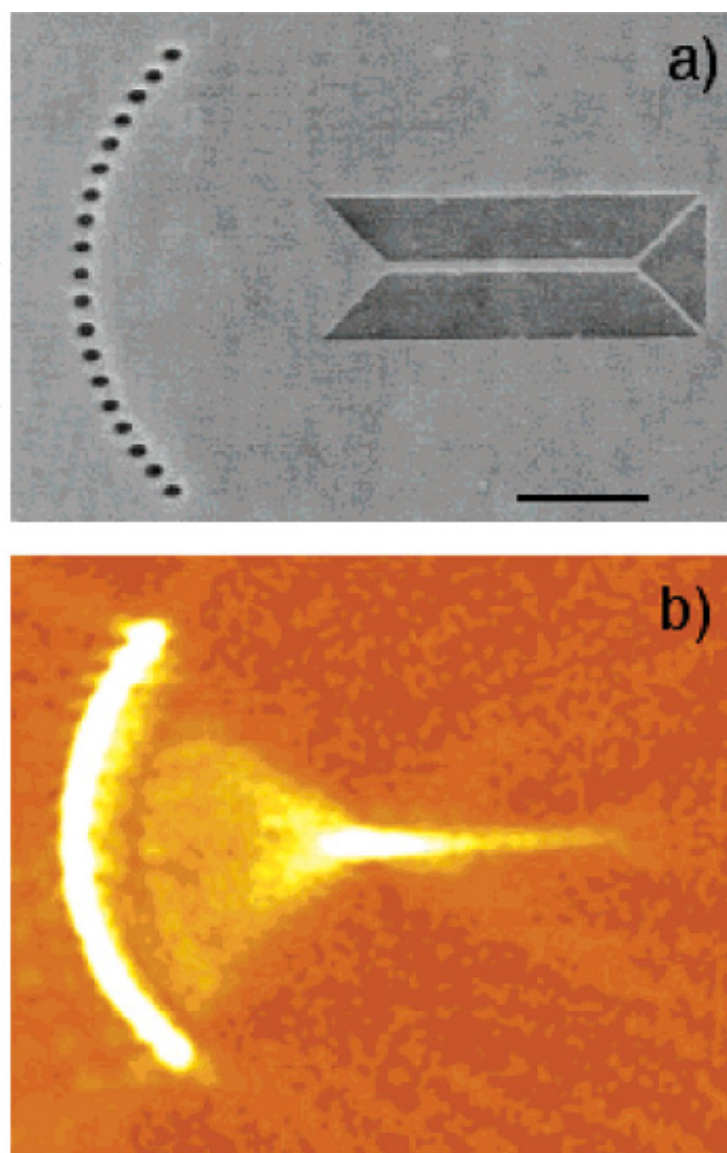


**Figure 35.** (a) SEM image of the focusing array coupled to a 250-nm-wide Ag strip guide; light gray, Ag; dark gray, Cr; scale bar, 2  $\mu\text{m}$ . (b) NSOM image of the SPPs intensity showing focusing and guiding. Reprinted with permission from “Leilei Yin, et. al., *Nano Lett.* 2005, 5, 1399–1402.” of copyright ©2005 Chemical Society of American.

a type of imaging by diffraction rather than an ordinary imaging of a lens. Actually, some researchers are still interested in the self-imaging effect since H. F. Talbot discovered it in 1836. And intensive theoretical and experimental studies regarding Talbot effect have been done since then. For example, the plasmon analogue of the self-imaging Talbot effect of a row of holes drilled in a metal film was described and theoretically analyzed, and suggested the potential applications in sensing, imaging, and optical interconnects on the basis of plasmon focal spots aimed at plasmon waveguides [63]. Subsequently, the Talbot effect regarding SPPs imaging on the basis of a rather different system by a quite different approach was studied theoretically and experimentally [62–64]. Furthermore, the Talbot effect for volume electromagnetic waves has been used in a variety of applications. And it is expected that the analogue for SPPs will be found applications in numerous nanoscale plasmonic devices.

Here, as an example, the Talbot effect of an Ag nanolens with five periodic concentric rings illuminated by a radially polarized light was computationally studied. Rigorous finite-difference and time-domain (FDTD) algorithm was employed in the computational numerical calculation. The results indicate that several focal points can be obtained at different locations due to the SPPs-related Talbot effect at  $\lambda_{inc.}=248$  nm. The positions are quite different from that of values calculated by the Talbot distance equation reported in Ref. [65]. A minimum diameter of 100 nm at site of full width and half maximum (FWHM) was derived at the propagation distance of  $Z=396$  nm. To further study the phenomenon in physics, it was compared with the traditional Talbot distance calculated using the scalar diffraction theory in the sections below.

For simplification of the analyses, the structure is simplified that is equivalent to a one-dimensional grating structure with the same geometrical parameters as the nanolens mentioned before due to its symmetry, as shown in Fig. 36.

The scalar field immediately behind an infinite grating at the original position ( $Z = 0$ ) when it is illuminated by an unit intensity plane wave can be described by a Fourier series representing a weighted set of plane wave components as:

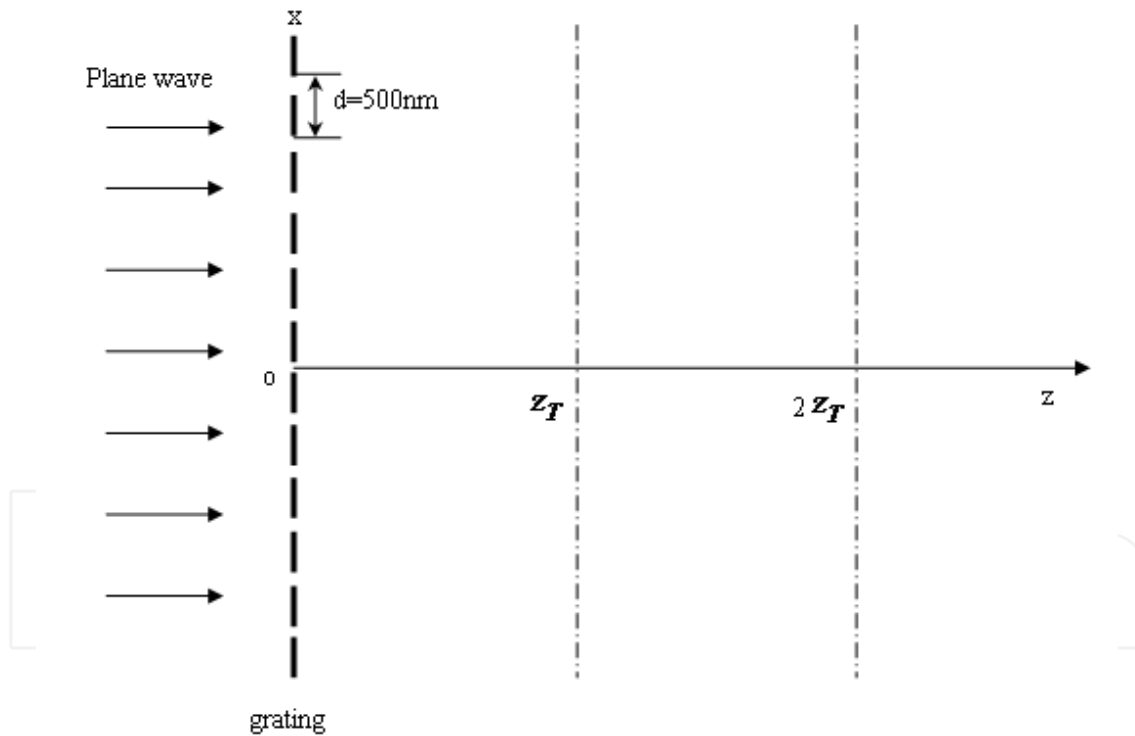


**Figure 36.** Self-imaging of the grating structure with the same geometrical parameters as the nanolens mentioned before.

$$U(x) = \sum_{n=-\infty}^{\infty} c_n \exp\left(j2\pi \frac{n}{d} x\right) \quad (7)$$

where  $d$  is the grating period (is 500 nm here) and  $c_n$  is the  $n^{\text{th}}$  Fourier coefficient. The coefficients represent the complex intensity and the phase.

According to the frequency domain analysis method, the diffraction field distribution  $U_z$  at a free-space propagation distance  $Z$  is given by

$$U_z(x) = \sum_{n=-\infty}^{\infty} c_n \exp\left(j2\pi \frac{n}{d} x\right) \exp\left[-j\pi\lambda z \left(\frac{n}{d}\right)^2\right] \exp(jkz) \quad (8)$$

Note that when

$$z = \frac{2md^2}{\lambda} \quad (m = 1, 2, 3, \dots) \quad (9)$$

then

$$\exp\left[-j\pi\lambda z \left(\frac{n}{d}\right)^2\right] = 1 \quad (10)$$

$U_z$  can be written as

$$U_z(x) = \sum_{n=-\infty}^{\infty} c_n \exp\left(j2\pi \frac{n}{d} x\right) \exp(jkz) = U(x) \exp(jkz) \quad (11)$$

Intensity distribution equals to the original intensity

$$I = |U_z(x)|^2 = |U(x)|^2 \quad (12)$$

The Talbot distance of a grating with a period of  $d$  is

$$z_T = \frac{2d^2}{\lambda} \quad (13)$$

Substituting  $d$  and  $\lambda$  with their corresponding values of 500 nm and 248 nm, respectively, we can get the Talbot distance of  $z_T = 2.016 \mu\text{m}$ . It indicates that self-imaging of the periodic grating structures can be observed at positions of  $Z = 2.016 \mu\text{m}$ ,  $4.032 \mu\text{m}$ , and  $6.048 \mu\text{m}$ , etc., which is integral number times of  $z_T$ .

It was found that the result analyzed above by the scalar diffraction theory is quite different from the results calculated by the FDTD numerical analysis method. The former is far field diffraction, but the latter is SPPs coupling and interfering at near field. Thus the focal points do not repeat at the same positions as that of the scalar one along the propagation direction. The phenomenon described before can be attributed to that of the surface plasmons (SP). SPPs is excited at all azimuthal directions that interferes each other constructively and creates a strongly enhanced localized fields at the focal points. The size of the focal spots is less than half a wavelength and the focal positions are not determined by the Talbot distance.



In comparison to the results of above mentioned Talbot distances from scalar theory, only the contribution from the field of SPPs is taken into account in the calculations of the interference pattern. In the geometry considered in this paper, the conversion of the incident SPPs into the volume electromagnetic waves is weak. The Talbot distance of  $2.016\ \mu\text{m}$  (first order) calculated by formula  $z_T = k\Lambda^2/\pi$  (it is the same as Eq. (13) actually. They were written in two different forms.) from Maradudin *et. al.* [63] and van Oosten [64] is different also from our calculated value of  $0.3962\ \mu\text{m}$  (first order) here. The reason we get a different answer compared to the other two methods is because the other two methods use the paraxial approximation in far-field regime, which state that the pitch of the structure is much greater than the incident wavelength. However, the near-field regime in which we operate is when the wavelength is about half the period. For our structures, the paraxial approximation does not hold anymore. Therefore, we can draw a conclusion that the theoretical equations deduced for the structures of metallic dot arrays [63, 65] are not suitable to our nanolens structures. The approach of computational numerical calculation must be employed for the study of the Talbot distance. For more information regarding theoretical calculation, readers can see Ref.[65].

To compare the experimental results with the theoretically calculated results, we plotted E-field intensity profiles versus propagation distance  $z$  together with that of the numerically calculated in the same figure, as shown in Fig. 37. It can be seen that variation tendency of the E-field intensity of the measured results is in agreement with the theoretically calculated results in general. As can be seen from Fig. 36, the positions of the measured first three focal points are slightly in advance of the calculated values due to the interaction of the metal surfaces between the NSOM probe and nanolenses at near-field. But for the last two ones,

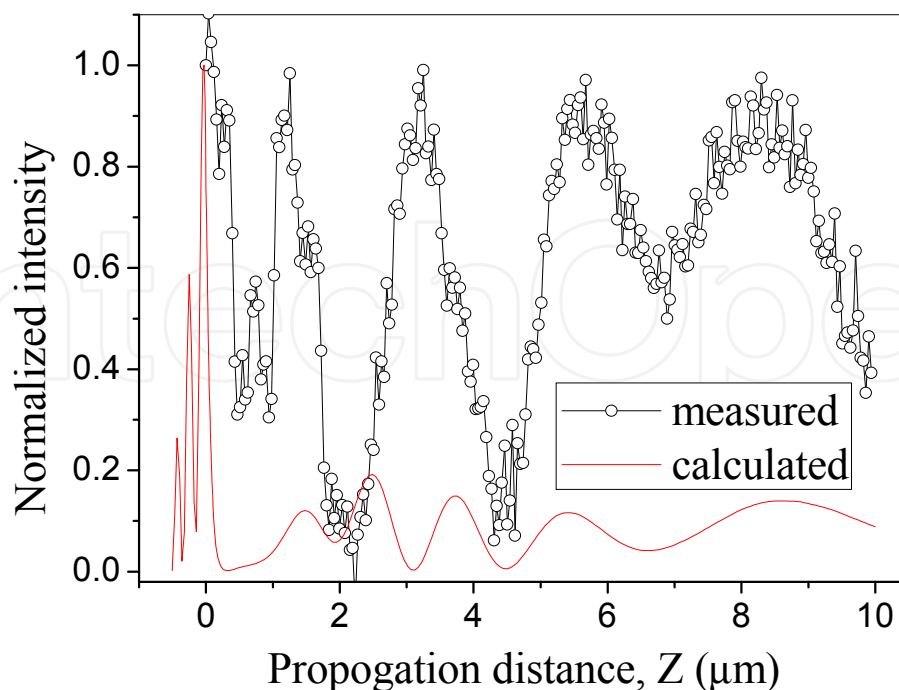


**Figure 37.** Comparison of E-field intensity distribution along propagation axis between experimental and theoretical results.

the measured and calculated results coincide with each other very well. It can be explained that the interaction between the NSOM probe and the nanolenses surface is weak at the far-field. The influence on the probing is significantly degraded and can be ignored accordingly.

In comparison to a standard diffraction experiment, if the wavelength is large the slit is subwavelength, surely there will be no diffracted waves (also known as cylindrical waves) and therefore, the distinction between short wavelength and long wavelength is obvious. For the standard diffraction, transmission intensity decays exponentially with slit size (Bethe's theory was put forth in 1944). However, for our plasmonic lenses, the transmission intensity can be enhanced due to inherent advantage of plasmonic resonance which is well known already. Here, we used metallic subwavelength structure to generate the self-imaging. It is more apparent in near field region. The contribution of plasmonic resonance here is that enhancing the intensity of the plasmonic Talbot-based focusing (see Fig. 36). It is especially important for nano-photolithography for which large working distance and high exposure intensity are crucial issues. Our previous FDTD calculation results [66] demonstrated that only one focal point can be observed for the case of  $\lambda > 300$  nm, which is a threshold value for the SPPs-based Talbot effect. For the short wavelength, it is smaller than the slit width. Thus it is consistent to the Talbot effect condition. For more information regarding experimental characterization, readers can see Ref.[67].

## 7. Summary

In summary, the main reason of the diffraction limit of a conventional optical lens is that a conventional lens is only capable of transmitting the propagating. The evanescent carry subwavelength information about the object decay, but it decay exponentially and cannot be collected in far field region. In contrast, plasmonic lens is an alternative to these problems. There are two key concepts about plasmonic lens. One is the concept of negative refractive index. The other is the transmission enhancement of evanescent waves. The concept of negative refractive index is the basic issue of plasmonic lens. And this is very common for noble metal in specific frequency.

The scalar Talbot effect cannot interpret the Talbot effect phenomenon for the metallic nanolenses. It may attribute to the paraxial approximation applied in the Talbot effect theory in far-field region. However, the approximation does not hold in our nanolenses structures during the light propagation. In addition, the Talbot effect appears at the short wavelength regime only, especially in the ultra-violet wavelength region.

Also plasmonic lenses provide excellent optical property for us. We can shape the beam beyond the diffraction limit, such as superfocusing, imaging and so on. Also we can exist in various forms. And in this paper, we show them in three form generally. Some new ideas will be produced while we design the plasmonic lenses to resolve practical problems. Currently, applications of the plasmonic lenses reported include photodetector [67] and ring resonator [68]. With rapid development of the plasmonic lenses, it is reasonable to believe that extensive applications will be found in the near future.

## Author details

Yongqi Fu

*School of Physical Electronics, University of Electronic Science and Technology of China, China*

Jun Wang and Daohua Zhang

*School of Electronic and Electrical Engineering, Nanyang Technological University, Republic of Singapore*

## Acknowledgement

Some reported research works in this chapter were supported by National Natural Science Foundation of China (No. 11079014 and 61077010).

## 8. References

- [1] J. B. Pendry, "Negative Refraction Makes a Perfect Lens", *Phys. Rev. Lett.* 5, 3966-3969 (2000).
- [2] Anthony Grbic and George V. Eleftheriades, "Overcoming the diffraction Limit with a planar Left-Handed Transmission-Line Lens", *Phys. Rev. Lett.* 92, No. 11, 117403 (2004).
- [3] D.R. Smith, J.B. Pendry, M.C.K. Wiltshire, "Metamaterials and negative refractive index", *Science* 305, 788-792 (2004).
- [4] S. Anantha Ramakrishna, "Physics of negative refractive index materials", *Rep. Prog. Phys.* 68 (2), 449-521 (2005).
- [5] T. W. Ebbesen, H. J. Lezec, H. F. Ghaemi, T. Thio and P. A Wolff, "Extraordinary optical transmission through subwavelength hole array", *Nature* 391, 667-669 (1998).
- [6] H.J. Lezec, A. Degiron, E. Devaux, R.A. Linke, F. Martín-Moreno, L.J. García-Vidal, and T.W. Ebbesen, "Beaming light from a subwavelength aperture", *Science* 297, 820 (2002).
- [7] Liang-Bin Yu, Ding-Zheng Lin et al., "Physical origin of directional beaming emitted from a subwavelength slit", *Phys. Rev. B* 71, 041405 (2005).
- [8] W. L. Barnes, A. Dereux, and T. W. Ebbesen, "Surface plasmon subwavelength optics", *Nature* 424, 824-830 (2003).
- [9] N. Fang, X. Zhang, "Imaging properties of a metamaterial superlens", *Appl. Phys. Lett.* 82(2), 161-163 (2003).
- [10] N. Fang, H. Lee, C. Sun and X. Zhang, "Sub-Diffraction-Limited Optical Imaging with a Silver Superlens", *Science* 308, 534-537 (2005).
- [11] Z. Liu, S. Durant, H. Lee, Y. Pikus, N. Fang, Y. Xiong, C. Sun, and X. Zhang, "Far-Field Optical Superlens", *Nano Lett.* Vol. 7, No. 2, 403-408 (2007).
- [12] N. Fang, Z. W. Liu, T.J. Yen, X. Zhang, "Regenerating evanescent waves from a silver superlens", *Opt. Express* 11(7), 682-687 (2003).
- [13] Z. W. Liu, J. M. Steele, W. Srituravanich, Y. Pikus, C. Sun, and X. Zhang, "Focusing surface plasmons with a plasmonic lens", *Nano Lett.* 5, 1726-1729 (2005).
- [14] D.O.S. Melville, R.J. Blaike, C.R. Wolf, "Submicron imaging with a planar silver lens", *Appl. Phys. Lett.* 84(22), 4403-4405 (2007).

- [15] Salandrino and N. Engheta, "Far-field Subdiffraction Optical Microscopy Using Metamaterial Crystals: Theory and Simulations", *Phys. Rev. B* 74, 075103 (2006).
- [16] W. Nomura, M. Ohtsu, and T. Yatsui, "Nanodot coupler with a surface plasmon polariton condenser for optical far/near-field conversion", *Appl. Phys. Lett.* 86, 181108 (2005).
- [17] Liang Feng, A. Kevin Tetz, Boris Slutsky, Vitaliy Lomakin, and Yeshaiah Fainman, "Fourier plasmonics: diffractive focusing of in-plane surface plasmon polariton waves", *Appl. Phys. Lett.* 91, 081101 (2007).
- [18] Z. Liu, H. Lee, Y. Xiong, C. Sun and X. Zhang, "Far-Field Optical Hyperlens Magnifying Sub-Diffraction-Limited Object", *Science* 315, 1686 (2007).
- [19] A. V. Zayats, I. I. Smolyaninov, and A. A. Maradudin, "Nano-optics of surface plasmon polaritons", *Phys. Rep.* 408, 131-314 (2005).
- [20] L. Zhou and C. T. Chan, "Relaxation mechanisms in three-dimensional metamaterial lens focusing", *Opt. Lett.* 30, 1812 (2005).
- [21] H. Ditlbacher, J. R. Krenn, G. Schider, A. Leitner, F. R. Aussenegg, "Two-dimensional optics with surface plasmon polaritons", *Appl. Phys. Lett.* 81, 762-764 (2002).
- [22] Yongqi Fu, W. Zhou, L.E.N. Lim, C. Du, H. Shi, C.T Wang and X. Luo, "Transmission and reflection navigated optical probe with depth-tuned surface corrugations", *Appl. Phys. B* 86, 155-158 (2007).
- [23] H. F. Shi, C. T. Wang, C. L. Du, X. G. Luo, X. C. Dong, and H. T. Gao, "Beam manipulating by metallic nano-slits with variant widths", *Opt. Express* 13, 6815-6820 (2005).
- [24] Avner Yanai and Uriel Levy, "The role of short and long range surface plasmons for plasmonic focusing applications", *Opt. Express* 17, No. 16 (2009).
- [25] M. H. Wong, C. D. Sarris, and G. V. Eleftheriades, "Metallic Transmission Screen For Sub-Wavelength Focusing", *Electronics Letters*, 43, 1402-1404 (2007).
- [26] Yongqi Fu, Wei Zhou, Lennie E.N. Lim, Chunlei Du, Haofer Shi, Changtao Wang, "Geometrical characterization issues of plasmonic nanostructures with depth-tuned grooves for beam shaping". *Opt. Eng.* 45, 108001 (2006).
- [27] Baohua Jia, Haofer Shi, Jiafang Li, Yongqi Fu, Chunlei Du, and Min Gu, "Near-field visualization of focal depth modulation by step corrugated plasmonic slits", *Appl. Phys. Lett.* 94, 151912 (2009).
- [28] Y. Xie, A.R. Zakharian, J.V. Moloney, and M. Mansuripur, Transmission of light through slit apertures in metallic films. *Optics Express*. 12. 6106-6121, (2004).
- [29] L.B. Yu, D.Z. Lin, Y.C. Chen, Y.C. Chang, K.T. Huang, J.W. Liaw, J.T. Yeh, J.M. Liu, C.S. Yeh, and C.K. Lee, Physical origin of directional beaming emitted from a subwavelength slit. *Physical Review B - Condensed Matter and Materials Physics*. 71. 1-4, (2005).
- [30] B. Ung and Y. Sheng, "Optical surface waves over metallo-dielectric nanostructures: Sommerfeld integrals revisited". *Optics Express*. 16. 9073-9086, (2008).
- [31] H. Shi, C. Du, and X. Luo, "Focal length modulation based on a metallic slit surrounded with grooves in curved depths". *Applied Physics Letters*. 91, (2007).



- [32] Z. Sun and H.K. Kim, "Refractive transmission of light and beam shaping with metallic nano-optic lenses". *Applied Physics Letters*. 85. 642-644, (2004).
- [33] Yongqi Fu, W. Zhou, L.E.N Lim, C. Du, H. Shi, C. Wang and X. Luo, "Influence of V-shaped plasmonic nanostructures on beam propagation", *Appl. Phys. B* 86, 461-466(2007).
- [34] Zhaowei Liu, Jennifer M. Steele, Hyesog Lee, and Xiang Zhang, "Tuning the focus of a plasmonic lens by the incident angle", *Appl. Phys. Lett.* 88, 171108 (2006).
- [35] Jun Wang, Wei Zhou and Anand K. Asundi, "Effect of polarization on symmetry of focal spot of a plasmonic lens". *Opt. Express* 17, 8137-8143 (2009).
- [36] LievenVerslegers, PeterB.Catrysse, ZongfuYu, JustinS.White, Edward S.Barnard, Mark L.Brongersma, and Shanhui Fan, "Planar Lenses Based on Nanoscale Slit Arrays in a Metallic Film". *Nano Lett.* 9, 235-238 (2009).
- [37] Jennifer M. Steele , Zhaowei Liu , Yuan Wang, and Xiang Zhang, Resonant and non-resonant generation and focusing of surface plasmons using circular gratings. *Opt. Express* 14, 5664-5670 (2006).
- [38] Yongqi Fu, W. Zhou, L.E.N.Lim, C.L. Du, X.G.Luo, Plasmonic microzone plate: Superfocusing at visible regime, *Appl. Phys. Lett.* 91, 061124 (2007).
- [39] Yongqi Fu, Yu Liu, Xiuli Zhou, Zong Weixu, Fengzhou Fang, Experimental demonstration of focusing and lasing of plasmonic lens with chirped circular slits, *Opt. Express* 18 (4), 3438–3443 (2010).
- [40] Wang, J., Zhou, W., Li, E. P. & Zhang, D. H., Subwavelength focusing using plasmonic wavelength-launched zone plate lenses. *Plasmonics*, 6, 269-272 (2011).
- [41] Richards, B. & Wolf, E. Electromagnetic Diffraction in Optical Systems. II. Structure of the Image Field in an Aplanatic System. *Proc. Roy. Soc. Lond A*, Vol.253, No.1274, 358-379 (1959).
- [42] Yongqi Fu, Wei Zhou, Hybrid Au-Ag subwavelength metallic structures with variant periods for superfocusing, *J. Nanophotonics* 3, 033504 (22 June 2009).
- [43] Yongqi Fu, Wei Zhou, Lim Enk Ng Lennie, Nano-pinhole-based optical superlens, *Research Letter in Physics*, Vol.2008, 148505 (2008).
- [44] Yongqi Fu, Xiuli Zhou, Yu Liu, Ultra-enhanced lasing effect of plasmonic lens structured with elliptical nano-pinholes distributed in variant period. *Plasmonics*, 5 (2), 111-116 (2010).
- [45] Zhenkui Shi, Yongqi Fu, Xiuli Zhou, Shaoli Zhu, Polarization effect on focusing of a plasmonic lens structured with radialized and chirped elliptical nanopinholes. *Plasmonics* 5(2), 175-182 (2010).
- [46] Yu Liu, Yongqi Fu, Xiuli Zhou, Polarization dependent plasmonic lenses with variant periods for superfocusing. *Plasmonics*, 5(2), 117-123 (2010).
- [47] Gilad M.Lerman, Avner Yanai, and Uriel Levy, "Demonstration of nanofocusing by use of plasmonic lens illuminated with radial polarized light". *Nano Lett.* 9, 2139-2143 (2009).
- [48] Qiwen Zhan, "Cylindrical vector beams: from mathematical concepts to applications", *Advances in Optics and Photonics* 1, 1-57 (2009).

- [49] T. Xu, C. L. Du, C. T. Wang, and X. G. Luo, "Subwavelength imaging by metallic slab lens with nanoslits", *Appl. Phys. Lett.* 91, 201501 (2007).
- [50] A. Ono, J. Kato, S. Kawata, "Subwavelength optical imaging through a metallic nanorod array", *Phys. Rev. Lett.* 95, 267407 (2005).
- [51] P. A. Belov, Y. Hao, S. Sudhakaran, "Subwavelength microwave imaging using an array of parallel conducting wires as a lens", *Phys. Rev. B* 73, 033108 (2006).
- [52] Mark I. Stockman, "Nanofocusing of Optical Energy in Tapered Plasmonic Waveguides", *Phys. Rev. Lett.* 93, 137404 (2004).
- [53] Ewold Verhagen, Albert Polman, and L. (Kobus) Kuipers, "Nanofocusing in laterally tapered plasmonic waveguides", *Opt. Express* 16, 45-57 (2008).
- [54] A. B. Evlyukhin, S. I. Bozhevolny, A. L. Stepanov, R. Kiyan, C. Reinhardt, S. Passinger, and B. N. Chichkov, "Focusing and directing of surface plasmon polaritons by curved chains of nanoparticles", *Opt. Exp.* 15, 16667-16680 (2007).
- [55] I. P. Radko, S. I. Bozhevolnyi, A. B. Evlyukhin, and A. Boltasseva, "Surface plasmon polariton beam focusing with parabolic nanoparticle chains", *Opt. Express* 15, 6576-6582 (2007).
- [56] Leilei Yin, Vitali K. Vlasko-Vlasov, John Pearson, Jon M. Hiller, Jiong Hua, Ulrich Welp, Dennis E. Brown, and Clyde W. Kimball, "Subwavelength Focusing and Guiding of Surface Plasmons", *Nano Lett.* 2005, 5, 1399-1402.
- [57] Z. J. Sun and H. K. Kim, "Refractive transmission of light and beam shaping with metallic nano-optic lenses", *Appl. Phys. Lett.* 85, 642 (2004).
- [58] Z. J. Sun, "Beam splitting with a modified metallic nano-optics lens", *Appl. Phys. Lett.* 89, 26119 (2006).
- [59] H. Ko, H. C. Kim, and M. Cheng, "Light transmission through a metallic/dielectric nano-optic lens", *J. Vac. Sci. Technol. B* 26, 62188-2191 (2008).
- [60] S. Vedantam, H. Lee, J. Tang, J. Conway, M. Staffaroni, J. Lu and E. Yablonovitch, "Nanoscale Fabrication of a Plasmonic Dimple Lens for Nano-focusing of Light", *Proceeding of SPIE* 6641, 6641J (2007).
- [61] James A. Shackelford, Richard Grote, Marc Currie, Jonathan E. Spanier, and Bahram Nabet, "Integrated plasmonic lens photodetector", *Appl. Phys. Lett.* 94, 083501 (2009).
- [62] W. Srituravanich, L. Pan, Y. Wang, C. Sun, C. Bogy, and X. Zhang, "Flying plasmonic lens in the near field for high-speed nanolithography", *Nature Nanotech.* 3, 733-737 (2008).
- [63] Dennis M R, Zheludev N I and García de Abajo F J , "The plasmon Talbot effect," *Opt. Express*, 15, 9692-700 (2007).
- [64] D. van Oosten, M. Spasenovi, and L. Kuipers, "Nanohole Chains for Directional and Localized Surface Plasmon Excitation." *Nano Lett.* 10, 286-290 (2010).
- [65] A A Maradudin and T A Leskova, "The Talbot effect for a surface plasmon polariton," *New J. Phys.* 11, 033004 (2009).
- [66] Lingli Li, Yongqi Fu, Hongsheng Wu, Ligong Zheng, Hongxin Zhang, Zhenwu Lu, Qiang Sun, Weixing Yu, The Talbot effect of plasmonic nanolens, *Opt. Express*, 19(20), 19365-19373 (2011).

- [67] Yiwei Zhang, Yongqi Fu, Yu Liu, Xiuli Zhou, Experimental study of metallic elliptical nanopinhole structure-based plasmonic lenses. *Plasmonics*, 6(2), 219-226 (2011).
- [68] V. S. Volkov, S. I. Bozhevolnyi, E. Devaux, J.-Y. Laluet, and T. W. Ebbesen, "Wavelength selective nanophotonic components utilizing channel plasmon polaritons", *Nano Lett.* 7, 880 (2007).

IntechOpen

IntechOpen